ENGINEERING THE SPECTRAL REFLECTIVITY OF MULTILAYER THIN FILMS

by
ONUR DEMİREL

Submitted to the Graduate School of Engineering and Natural Sciences
in partial fulfilment of
the requirements for the degree of Master of Science

Sabancı University
May 2025

ENGINEERING THE SPECTRAL REFLECTIVITY OF MULTILAYER THIN FILMS

Approved by:

Prof. Dr. İBRAHİM KÜRŞAT ŞENDUR .....
(Thesis Supervisor)

Prof. Dr. FEVZİ ÇAKMAK CEBECİ .....

Asst. Prof. MUHAMMED ALİ KEÇEBAŞ .....

Date of Approval: May 28, 2025

ABSTRACT

ENGINEERING THE SPECTRAL REFLECTIVITY OF MULTILAYER THIN FILMS

ONUR DEMİREL

MECHATRONICS ENGINEERING M.A. THESIS, MAY 2025

Thesis Supervisor: Prof. Dr. İBRAHİM KÜRŞAT ŞENDUR

Keywords: electromagnetic spectrum, spectrally selective filters, distributed bragg reflectors, tunable reflectance

Achieving a high reflectance over the infrared bands has attracted interest due to potential applications in lasers and thermophotovoltaic devices. Additionally, structures that operate across multiple bands and provide spectrally selective broadband reflectivity are under investigation for various applications. Moreover, there has been a growing interest in recent years in studies aimed at achieving switchable radiation properties for thermal management, particularly in space applications. Distributed Bragg Reflectors are commonly used in applications that require high reflectivity, consisting alternating high-index and low-index dielectric thin films. They can be specifically designed for multi-band functionalities. In this study, the reflectivity of multilayer thin film structures was first examined separately for single band applications. The performance of Bragg Reflectors was enhanced through Tandem Approaches and optimization techniques. Both the Transfer Matrix Method and Finite Difference Time Domain methods were employed, allowing for the evaluation of the reliability of these design tools. Optimization studies were conducted using Impedance Mismatch-Based Optimization, a physics-based method which aims equalizing the absolute value of complex reflectivity to unity. The broadband reflectivity of thin multilayer thin films was assessed, and spectrally selective reflectance was pursued through further optimization. Finally, conical VO2 structures were employed to achieve tunable spectral reflectance, leveraging the phase change properties of VO2. The effects of geometric parameters—such as height, radius, and periodicity of the conical structures—on the optical response were investigated.

ÖZET

YANSITICI ÇOK KATMANLI İNCE FİLMLERİN TASARIMI

ONUR DEMİREL

Mekatronik Mühendisliği YÜKSEK LİSANS TEZİ, MAYIS 2025

Tez Danışmanı: Prof. Dr. İBRAHİM KÜRŞAT ŞENDUR

Anahtar Kelimeler: ayarlanabilir yansıtıcılık, Bragg yansıtıcıları, elektromanyetik tayf, seçici geçirgen filtreler

Kızılötesi bantlarda yüksek yansıma elde etmek, lazerler ve termofotovoltaik cihazlardaki potansiyel uygulamalar nedeniyle ilgi çekmiştir. Ek olarak, birden fazla bantta çalışan ve spektral olarak seçici geniş bant yansıtma sağlayan yapılar çeşitli uygulamalar için araştırılmaktadır. Son olarak, son yıllarda özellikle uzay uygulamalarında termal yönetim için anahtarlanabilir radyasyon özellikleri elde etmeyi amaçlayan çalışmalara artan bir ilgi olmuştur. Dağıtılmış Bragg Yansıtıcıları, yüksek yansıtma gerektiren uygulamalarda yaygın olarak kullanılan, yüksek kırınım indisli ve düşük kırınım indisli dielektrik ince filmlerin üst üste kullanıldığı yapılardır. Çok bantlı uygulamalara özel olarak tasarlanabilirler. Bu çalışmada, çok katmanlı ince film yapıların yansıtıcılığı ilk olarak tek bir spektral bölgenin hedeflendiği çalışmalarda ayrı ayrı incelenmiştir. DBR'lerin tek bantlı uygulamalardaki performansı, tandem yaklaşımı ve optimizasyon teknikleri ile geliştirilmiştir. Hem Transfer Matrisi Yöntemi hem de Zamanda Sonlu Farklar yöntemleri kullanılmış ve modelleme araçlarının güvenilirliği doğrulanmıştır. Optimizasyon çalışmaları, karmaşık yansıtıcılığın mutlak değerini bire eşitlemeyi amaçlayan fizik tabanlı bir yöntem olan Empedans Uyumsuzluğu Tabanlı Optimizasyon kullanılarak yürütülmüştür. Bragg Yansıtıcıları'nın geniş bant yansıtıcılığı değerlendirilmiş ve optimizasyon çalışmaları ilerletilerek spektral olarak seçici yansıma elde edilmiştir. Son olarak, VO2'nin faz değişim özelliklerini kullanarak, ayarlanabilir yansıma elde etmek için konik VO2 yapıları kullanılmıştır. Konik yapıların yüksekliği, yarıçapı ve periyodikliği gibi geometrik parametrelerin optik tepki üzerindeki etkileri araştırılmıştır.

To My Mother,

TABLE OF CONTENTS

LIST OF TABLES ix

LIST OF FIGURES x

1. INTRODUCTION 1

1.1 Literature Survey 4

1.2 Contributions 7

1.3 Outline 7

2. MWIR 9

2.1 Problem Definition 9

2.2 Modelling 10

2.2.1 Transfer Matrix Method 10

2.2.2 Finite Difference Time Domain 12

2.3 Design Methods 17

2.3.1 Quarter Wavelength Approach 17

2.3.2 Tandem Approach 20

2.3.3 Impedance Mismatch Based Optimization 21

2.4 Results 23

2.4.1 Quarter-Wavelength Approach 23

2.4.2 Tandem Approach 27

2.4.3 Impedance Mismatch Based Optimization 31

3. LWIR 33

3.1 Problem Definition 33

3.2 Results 36

3.2.1 Quarter-Wavelength Approach 36
3.2.2 Tandem Approach 38
3.2.3 Impedance Mismatch Based Optimization 40
3.2.4 Spectrally Selective Wide-Band Reflectance 44
3.3 Conclusion 47
4. TUNABLE REFLECTANCE 49
4.1 Problem Definition 49
4.2 Results 53
4.3 Conclusion 63
5. CONCLUSION & FUTURE WORK 64
5.1 Conclusion 64
5.2 Future Work & Limitations 66
BIBLIOGRAPHY 69

LIST OF TABLES

Table 1. Maxwell's Equations 12
Table 2. Average reflectance of SiO2 and varying number of layers..... 25
Table 3. Comparison of reflectivity values obtained with ideal and error-added thicknesses. 27
Table 4. Average reflectance of SiO2, 10-layered structure, Tandem-3.5 μm and Tandem-4.5 μm..... 30
Table 5. Thicknesses and average reflectance of two different data sets obtained using Impedance Mismatch Based Optimization 31
Table 6. Average reflectance and thickness of ZnS and varying number of layers..... 38
Table 7. Average reflectance of Tandem structures with varying number of layers..... 39
Table 8. Thickness of individual layers as outputs of optimization with respect to number of layers and upper bound for layer thickness 40
Table 9. Average reflectance and total thickness with respect to number of layers..... 42
Table 10. Average reflectance and total thickness with respect to number of layers..... 43
Table 11. Results of Quarter-Wavelength Approach, Tandem Approach and Impedance Mismatch Based Optimization..... 47

LIST OF FIGURES

Figure 1. Wave-matter interaction 1
Figure 2. Reflectance of a perfect MWIR reflector 9
Figure 3. Wave propagation in a layered media 10
Figure 4. Yee lattice or Yee grid 13
Figure 5. A fundamental FDTD algorithm 16
Figure 6. Light reflecting from different interfaces in a layered medium 18
Figure 7. Representation of constructive interference in a DBR 19
Figure 8. Dividing MWIR band and aiming high reflectance with two different layered mediums 20
Figure 9. Reflectance coefficient in complex impedance plane 22
Figure 10. Reflectance spectrum of 2, 4, 6, 8, 10 and 12-layered coatings obtained by TMM. 23
Figure 11. Reflectance spectrum of 2, 4, 6, 8, 10 and 12-layered coatings obtained by Lumerical. 24
Figure 12. Reflectance spectrum of substrate 10-layered structure obtained by TMM and Lumerical. 26
Figure 13. Reflectance spectrum of 10-layered structures that is designed addressing 3.5 μm and 4.5 μm. 28
Figure 14. Reflectance spectrum of Tandem - 3.5 um and Tandem 4.5 um 29
Figure 15. Reflectance spectrum of SiO_2, 10-layered structure, Tandem-3.5 μm and Tandem-4.5 μm 30
Figure 16. Reflectance spectrum of 9-layered structures with different thickness configurations that is obtained by Impedance Mismatch Based Optimization 32
Figure 17. Refractive indices of materials 34
Figure 18. Extinction coefficients of materials 34
Figure 19. Reflectance spectrum of ideal spectrally selective multiband filter 35

Figure 20. Reflectance spectrum of 2, 4, 6, 8, 10 and 12-layered coatings obtained by TMM. 36
Figure 21. Reflectance spectrum of 2, 4, 6, 8, 10 and 12-layered coatings obtained by FDTD. 37
Figure 22. Reflectance spectrum of 4, 8, 12, 16, 20-layered coatings designed by Tandem Approach 39
Figure 23. Reflectance spectrum of 4, 6, 8, 10, 12-layered coatings obtained by Impedance Mismatch Based Optimization with 2500 nm of upper limit for layer thickness 41
Figure 24. Reflectance spectrum of 4, 6, 8, 10, 12-layered coatings ontained by Impedance Mismatch Based Optimization with 1500 nm of upper limit for layer thickness 43
Figure 25. Broadband reflectance spectrum of LWIR design 45
Figure 26. Broadband reflectance spectrum optimized structure 46
Figure 27. Refractive index of VO_2 in metallic and insulator phases 49
Figure 28. Extinction coefficients of VO_2 in metallic and insulator phases 50
Figure 29. Reflectivity difference between two states 51
Figure 30. VO_2 cones on DBR 52
Figure 31. Parameters of VO_2 cones 52
Figure 32. Reflectance spectrum of DBR in NIR 53
Figure 33. Reflectance spectrum of DBR+VO_2 with varying cone diameter 54
Figure 34. Reflectance spectrum of DBR+VO_2 with varying cone diameter 54
Figure 35. Reflectance spectrum of DBR+VO_2 with varying cone height 55
Figure 36. Reflectance spectrum of DBR+VO_2 with varying cone height 56
Figure 37. Reflectance spectrum of DBR+VO_2 with varying periodicity 57
Figure 38. Reflectance spectrum of DBR+VO_2 with varying periodicity 57
Figure 39. Reflectance spectrum of the structure when VO_2 is in different phases 58
Figure 40. Transmittance spectrum of DBR+VO2 in absorber/emitter mode 59
Figure 41. Reflectance spectrum of DBR + VO2 film when VO2 is in different phases 60
Figure 42. E-field Distribution at 1500 µm 61
Figure 43. E-field Distribution at 1750 µm 61
Figure 44. E-field Distribution at 2000 µm 62
Figure 45. E-field Distribution at 2250 µm 62

Figure 46. E-field Distribution at 2500 μm 63

1. INTRODUCTION

Controlling the interaction of electromagnetic radiation with matter has led to the development of many technologies. In many independent fields such as communication technologies, imaging techniques, biomedical, thermal management, it is aimed to manipulate electromagnetic radiation at different frequencies.

In this thesis, studies are conducted on the design, efficiency and functionality of Distributed Bragg Reflectors (DBR), which are utilized for a long time to achieve high reflectivity, in other words, to manipulate the electromagnetic radiation in the infrared band. To examine and optimize reflection, it is beneficial to delve into the underlying physical principles of the phenomenon.

Electromagnetic waves, upon encountering materials, engage in a trifold manner of interaction: reflection, wherein waves are bounced back; absorption, where waves are internalized by the material; and transmission, allowing waves to pass through the material.

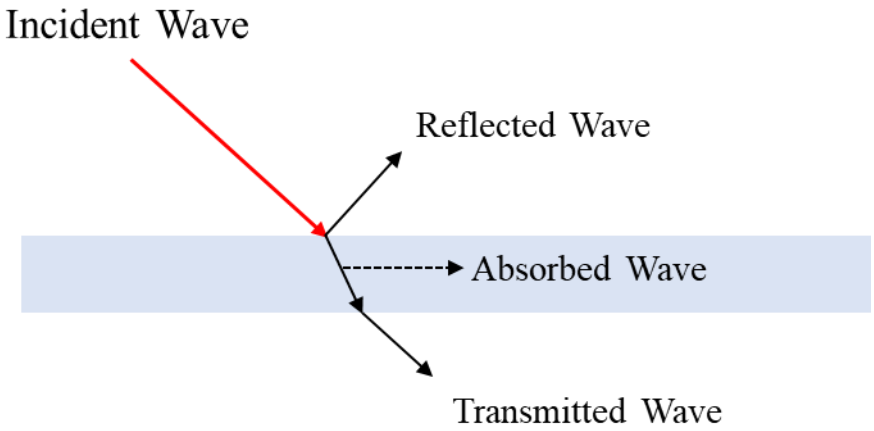

Figure 1. Wave-matter interaction

The law of conservation of energy dictates that the energy of the incident wave must equal the sum of the energies of the reflected, absorbed, and transmitted waves by the matter. This condition is expressed as Eq. (1.1).

$$I_{Incident} = I_{Reflected} + I_{Absorbed} + I_{Transmitted} \tag{1.1}$$

Another pertinent law that may prove beneficial is the Kirchhoff's Law of Thermal Radiation, articulated as Eq. (1.2) (Howell et al., 2020). This law asserts that for a body in thermal equilibrium, the intensity of absorbed and emitted waves is equal.

$$emissivity\ (\lambda, T) = \ absorptivity\ (\lambda, T) \tag{1.2}$$

These laws outline the fundamental principles necessary to achieve a reflective structure. Maximizing reflectance can also be accomplished by minimizing transmittance and emissivity/absorptivity under thermal equilibrium.

Manipulating the interaction of electromagnetic waves with matter according to these principles has led to the development of many technologies. For example, technologies based on maximizing the absorption of electromagnetic radiation include solar panels, bolometers in infrared detectors, and EMI/RFI absorbers developed to prevent interference in electronic devices. Structures that reflect electromagnetic radiation at high levels are used in laser systems, spacecraft thermal management, and low-visibility technologies.

In technologies based on electromagnetic wave–matter interactions, the objective is generally to maximize the desired response at the target wavelength. For example, EMI absorbers are designed to exhibit maximum absorption at specific wavelengths and, depending on the application, to maintain this performance across multiple wavelength ranges. Similarly, in laser systems employing distributed Bragg reflectors (DBRs), achieving high reflectivity with lower cost and fewer layers can lead to increased system efficiency.

Distributed Bragg Reflectors (DBRs) are structures commonly used in applications requiring high reflectivity in the visible and infrared spectral bands. They consist of alternating layers of high- and low-refractive-index dielectric materials. Traditional

design approaches can achieve high levels of reflectivity when appropriate materials are selected. However, these methods also impose limitations on the efficiency of DBRs, as increasing the number of layers is the only available strategy to enhance reflectivity. Moreover, conventional design techniques have not allowed for significant diversification of the capabilities of these structures, despite their long-standing use. In the Literature Survey section, general applications of reflective structures are discussed, along with scientific studies addressing the performance and efficiency of DBRs. Additionally, studies aimed at enhancing the functionality of DBRs are examined. The review aims to identify both the achievements reported in the literature and areas with potential for further development.

It is anticipated that design schemes and physics-based optimization methods, which have been applied in various technologies involving electromagnetic wave–matter interactions, may be beneficial for re-evaluating the efficiency limits of DBR structures and enhancing their functionality.

Section 2 begins by focusing on reflectors designed for the MWIR band, examining the performance of the traditional quarter-wavelength approach in this spectral range. Subsequently, alternative design strategies are introduced to validate the proposed hypothesis. New multilayer stacks are then developed using the Tandem approach—commonly employed in solar panel design—and impedance mismatch-based optimization, a physics-based method. The performances of these approaches are compared with that of the traditional method. The underlying principles of the modeling techniques used for DBRs throughout the study are presented in Section 2.2, Modeling. Section 2.3, Design Methods, outlines the theoretical foundations of the design strategies applied in both the MWIR and LWIR bands.

In Section 3, the study is extended to the LWIR band. It is demonstrated that the traditional design approach remains effective in this wavelength range when appropriate materials are used. Similar to the previous section, the efficiency of various design strategies is evaluated. Given the flexibility of the optimization method, which can be configured to target different spectral bands, the feasibility of developing spectrally selective filters that provide high reflectivity in both the MWIR and LWIR bands is investigated.

In Section 4, materials science was incorporated to enhance the functionality of DBRs. In this part of the study, conical VO_2 structures were integrated into DBRs exhibiting high reflectivity. The objective was to modulate reflectivity by leveraging the phase-change properties of VO_2. Section 4.1, Problem Definition, outlines the functional characteristics of VO_2. Additionally, relevant studies in literature are discussed, with a focus on the switchability and performance benefits of conical structures. Section 4.2, Results, presents the simulation outcomes. Finally, the physical mechanisms underlying the reflectivity distributions achieved using these conical structures are analyzed.

1.1 Literature Survey

The infrared spectrum is divided into sub-bands in different ways. The wavelength ranges of 0.7-2.5 μm, 3-5 μm and 8-14 μm are called Near-Infrared (NIR), Mid-Wave Infrared (MWIR) and Long-Wave Infrared (LWIR), respectively (Kyal et al., 2018). High reflectivity has been attempted to be achieved both by targeting these sub-bands one by one and within the scope of multiband applications.

Achieving strong MWIR reflectivity has attracted interest in various applications including spectrally selective filters (Shim et al., 2022), lasers (Williams et al., 2020), photodetectors (Letka et al., 2019), chemical spectroscopy (Bergthold et al., 2022) and radiative cooling (Wang et al., 2022). LWIR reflectivity is useful in applications like energy efficiency in buildings (Dang et al., 2020) and photodetectors (Long et al., 2019). Additionally, NIR reflectivity has investigated light-emitting diodes (LEDs) (Lee et al., 2024), and vertical cavity surface-emitting lasers (VCSELs) (Liu et al., 2020) utilize Bragg reflectors. Furthermore, structures that operate across multiple bands and provide spectrally selective broadband reflectivity are under investigation for various applications (Gill et al., 2022).

Different methods can be utilized to achieve high infrared reflectivity. The first solution is to use metals. Copper and aluminum provide reflectivity above approximately 0.8 in the wavelength range of 1-20 μm (Quazi et al., 2016). Another common solution is Distributed Bragg Reflectors.

A distributed Bragg reflector DBR is composed of alternating high index/low index dielectric multilayer thin films and is one of the most common radiation engineering tools that enhances reflectivity. Geometry parameters and material types in these multilayer thin films are selected to promote constructive and destructive interference that leads to reflectivity and emissivity engineering in different spectral bands.

DBRs have been used in optical components for years. The traditional design method is adjusting the layer thickness with quarter-wavelength approach to maximize reflectivity around the targeted wavelength. As the number of layers increases, reflectivity improves correspondingly. However, each layer in the DBR structure contributes to additional time and cost. Reducing the number of layers enhances resource efficiency and results in more compact structures. In this study, the performance of DBRs was analyzed for single-band and subsequently multiband applications, with the aim of improving their efficiency.

A review of the literature reveals that high reflectivity has been achieved in the visible, NIR, MWIR, and LWIR bands using traditional methods. The following studies can be given as examples for studies in the visible band. Sugawara et al. (1993) achieved approximately 84% reflectivity using 20 film pairs (i.e., approximately 40 layers) composed of InGaAlP and GaAs. Rissanen et al. (2012) obtained over 80% reflectivity with only 5 layers by employing Al_2O_3/TiO_2 films in Fabry–Perot interferometers. Dubey et al. (2017) reported 0.9 reflectance in the visible region using a structure consisting of 7 pairs of TiO_2 and SiO_2, designed for light-trapping applications. Leem et al. (2014) employed a novel fabrication approach by stacking high-index and low-index layers using TiO_2 films with different structures—specifically, high-density TiO_2 and hollow-structured TiO_2 films. Using this configuration, they achieved over 0.9 reflectance in the visible wavelength range with just 5-layer pairs. Increasing the number of pairs to 8 further enhanced the reflectivity to approximately 0.99.

Similar examples can be given for infrared wavelengths. Lee et al. (2024) achieved 0.96 reflectance at wavelength of 850 nm using 20 pairs of $Al_{0.9}Ga_{0.1}As$ and $Al_{0.1}Ga_{0.9}As$ thin films in their study on various reflective systems. Mrazek et al. (2021) reported approximately 0.97 reflectance at 980 nm with DBR structures composed of 8 film pairs of Zn_2TiO_4 and amorphous porous SiO_2, fabricated using the sol-gel method. everal studies have reported higher reflectivity levels in the MWIR band. Fan et al. (2012) achieved approximately 99.9% reflectivity using 10 pairs of ZnTe/GaSb films. Mikulicze

et al. (2024) reported approximately 97% reflectivity at a wavelength of 4 μm with 12 DBR pairs. Tripathi et al. (2015) developed reflective structures composed of silicon and air layer pairs for use in Fabry–Perot filters. They employed a multi-step fabrication process in which they achieved 0.94 reflectance. Reflectance studies in the LWIR band have been found to be more limited compared to those in other spectral regions. Gill et al. (2022) achieved approximately 0.97 reflectance in an air-gapped structure through the application of several fabrication steps. In their theoretical study, Ko et al. (2024) developed metasurfaces using particle swarm optimization and achieved near-100% reflectance.

An evaluation of the studies suggests that achieving reflectivity levels of 0.90 or higher generally requires at least 20 film layers. It is also evident that the fabrication process tends to become more complex as efficiency of the structures increases.

The LWIR band can also be targeted in studies aiming to develop multiband spectrally selective filters. Xie et al. (2025), in their study focused on designing a selective emitter, achieved high reflectivity in both the MWIR and LWIR bands using a 16-layer structure. Similarly, Xu et al. (2024) developed a multiband emitter optimized through a genetic algorithm-based method. Although specific reflectivity values were not reported in their study, the emittance graphs suggest that a certain level of reflectivity was attained in the MWIR and LWIR regions.

Another interesting issue is the addition of different functionalities to traditional design schemes. For example, the ability to adjust reflectivity properties during use with various mechanisms has been investigated in recent years for the purpose of using them in the thermal management of spacecraft (Kong et al., 2024). In the last part of the thesis, studies on this subject are detailed a little more, and an attempt is made to contribute to the literature by combining traditional DBR structures and innovative approaches

1.2 Contributions

The aim of this thesis is to improve the single-band and multi-band performances of traditional DBR structures and to provide functionality. Contributions to current literature are listed below.

- DBR performance in MWIR and LWIR bands is investigated using different design approaches. The performance and efficiency of the structures are improved.
- Spectrally selective structures are developed using the optimization method and it is shown that the method is suitable for designs to be used in multi-band applications.
- Functionality is added to traditional DBR structures by utilizing the properties of the phase change material VO_2 and adjustable reflectivity is achieved in NIR.

1.3 Outline

In chapter 2, the fundamentals of the methods used in modeling layered thin film structures are discussed. Briefly, the mathematics on which the Transfer Matrix Method (TMM) and Finite Difference Time Domain (FDTD) methods are based are explained. Then, the fundamentals of the design approaches are explained. Quarter-Wavelength and Tandem Approaches and Impedance Mismatch-Based Optimization technique are discussed, respectively. Reflective structures operating in the MWIR band are developed using the explained modeling techniques and design approaches and their performances are compared.

In chapter 3, MWIR studies are extended to the LWIR band. Similarly, the effects of different design approaches on LWIR reflectivity are examined.

In chapter 4, the usability of the optimization method, whose performance increase is examined in single band studies, is investigated for developing multiband designs. As a result of the studies, spectrally selective wideband reflectance is obtained.

In chapter 5, adjustable reflectance is obtained in the NIR band by using conical VO_2 structures on top of DBR structures. The effects of the geometric parameters of conical structures are investigated.

2. MWIR

2.1 Problem Definition

To achieve an ideal MWIR reflector with spectral reflectance as depicted in figure 2, it is possible to resort to methods that, in addition to maximizing reflection, minimize the transmittance properties or the absorbance/emittance of a material system in thermal equilibrium.

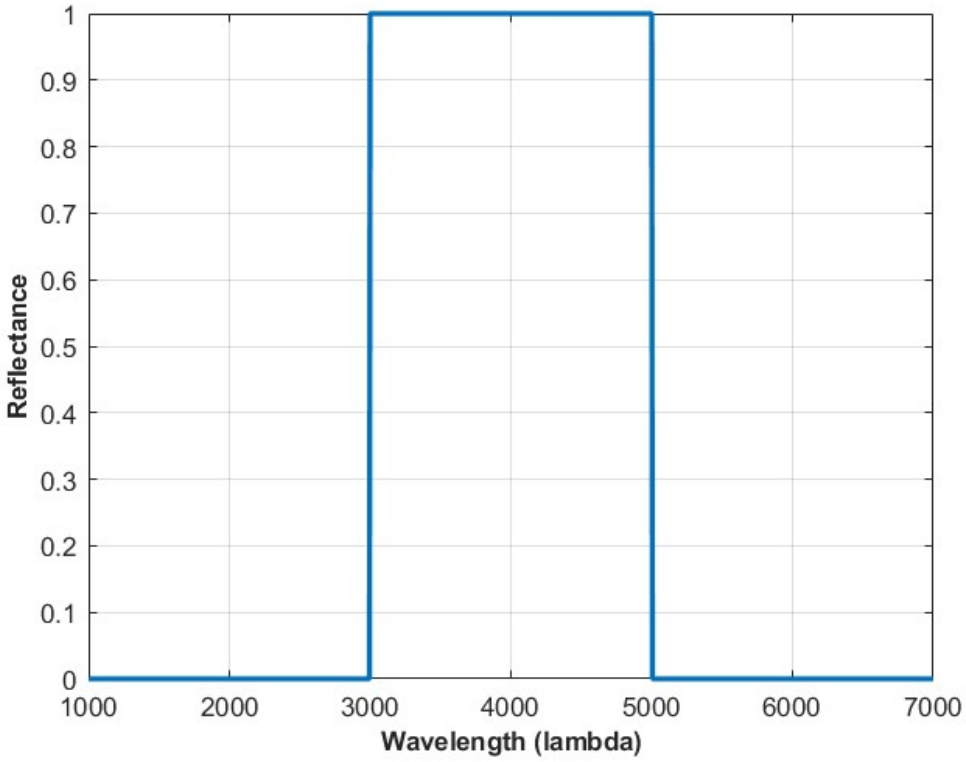

Figure 2. Reflectance of a perfect MWIR reflector

In the following sections, ways to model and analyze the interaction of electromagnetic waves and matter and design methods that can be used to obtain reflective structures will

be discussed. DBR designs will be developed and the efficiency of the structures will be examined.

2.2 Modelling

Both analytical and numerical methods are utilized for modelling the geometry. TMM is an analytical solution of Maxwell's Equations that behavior of electromagnetic waves in a layered medium can be predicted. MATLAB is preferred to perform TMM. Numerical solutions were obtained using FDTD in ANSYS Lumerical – FDTD software package. Analytical and numerical solutions were compared, and the effectiveness of tools were confirmed.

2.2.1 Transfer Matrix Method

Transfer Matrix Methods (TMM) analyzes propagation of electromagnetic or acoustic wave in one dimensional system. Based on the principle of electric field continuity at boundaries, it enables the possibility of conducting a highly useful analysis for the propagation of electromagnetic waves. (Markos et al., 2008)

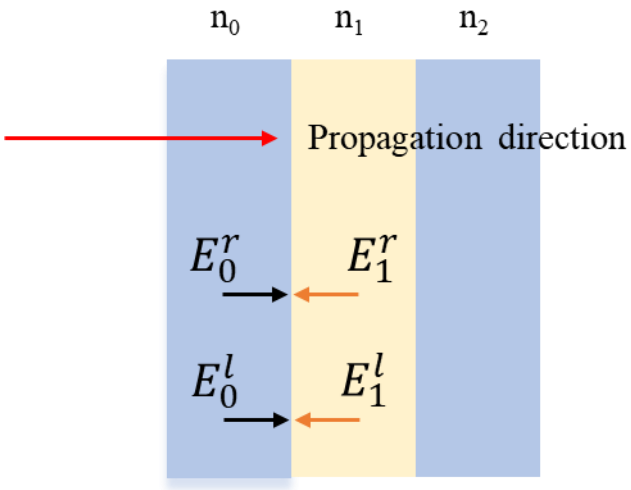

Figure 3. Wave propagation in a layered media

Electromagnetic wave that is propagating in a layered medium such as in figure 3 has an electric field component that can be represented as two individual electric field

subcomponents as E_0^r and E_0^l at just before the n_0-n_1 interface. Similarly, electric field just after the n_0-n_1 interface can be represented by two different subcomponents as E_1^r and E_1^l. Effect of n_0-n_1 interface on propagating wave while passing from n_0 to n_1 can be represented by a simple matrix operation. Similarly, effects of all interfaces in the layered structure can be represented by simple matrix operations. Furthermore, transformation of waves in individual mediums (n_0, n_1, …) can be represented with matrix operations. Matrices representing transformations at interfaces and in individual layers can be multiplied successively to find the relationship between the initial and final states of the electromagnetic wave in a layered structure. This allows the calculation of how the structure influences the wave.

In the following sections, formulas for obtaining the optical response of a multilayer thin film structure will be provided without derivations. Formulations are retrieved from Heavens (1986) and Keçebaş et al. (2016). Spectral behavior of a thin film system, as shown the figure 3, can be calculated using Eq. (2.1) under normal incidence.

$$\begin{bmatrix} B \\ C \end{bmatrix} = \begin{bmatrix} cos\delta & (isin\delta)/N_1 \\ iN_1 sin\delta & cos\delta \end{bmatrix} \begin{bmatrix} 1 \\ N_2 \end{bmatrix} \tag{2.1}$$

$$\delta = \frac{2\pi N d}{\lambda} \tag{2.2}$$

$$N = n - ik \tag{2.3}$$

In equations, δ is optical distance, N is complex refractive index, d is thicknesses of individual layers, λ is wavelength, n is refractive index, and k is extinction coefficient. B and C are the coefficients that can be used for obtaining total reflectance, absorptance and transmittance of the thin film system. The Eq. (2.1) can be extended to make calculations in a multi-layer system as follows:

$$\begin{bmatrix} B \\ C \end{bmatrix} = \prod_{r=1}^{q} \begin{bmatrix} cos\delta_r & (isin\delta_r)/N_r \\ iN_r sin\delta_r & cos\delta_r \end{bmatrix} \begin{bmatrix} 1 \\ N_m \end{bmatrix} \tag{2.4}$$

Total optical response of a thin film system under normal incidence can be obtained using following equations.

$$R = \left(\frac{N_0 B - C}{N_0 B + C}\right)\left(\frac{N_0 B - C}{N_0 B + C}\right)^* \tag{2.5}$$

$$T = \frac{4N_0 Re(N_m)}{(N_0 B + C)(N_0 B + C)^*} \tag{2.6}$$

$$A = \frac{4N_0 Re(BC^* - N_m)}{(N_0 B + C)(N_0 B + C)^*} \tag{2.7}$$

N_0, Nr and Ns are complex refractive indices of the incidence medium, individual layers and substrate respectively.

2.2.2 Finite Difference Time Domain

In this section, video and written materials of online lecture named "Electromagnetic Analysis Using Finite-Difference-Time-Domain" were used (Rumpf, 2021). Finite-Difference-Time-Domain (FDTD) method solves Maxwell's equations by discretizing the temporal and spatial derivatives. The Yee Grid method, developed by Kane S. Yee, is used as the discretization technique (Yee, 1966). Method can be utilized to analyze wave-matter interaction for various applications and wideband solutions can be obtained in a single simulation run.

Maxwell's equations consist of two curl and two divergence equations that form the foundation of classical electromagnetism and explain the behavior of electromagnetic waves. The differential form of these equations are as follows:

Table 1. Maxwell's Equations

Gauss Law	$\nabla . \vec{D} = \rho$
Gauss Law for Magnetism	$\nabla . \vec{B} = 0$
Faraday's Law of Induction	$\nabla \times \vec{E} = -\frac{\partial \vec{B}}{\partial t}$
Ampère's Law (with Maxwell's addition)	$\nabla \times \vec{H} = J_i + \frac{\partial \vec{D}}{\partial t}$

In equations, D is electric displacement field, B is magnetic induction, E is electric field, H is magnetic field intensity, ρ is electric charge intensity and Ji is current intensity. Material properties are involved into equations by constitutive relations. Constitutive relations for linear, isotropic, non-dispersive and homogenic materials are as follows:

$$\vec{D} = \varepsilon\vec{E}\ ,\ \vec{B} = \mu\vec{H} \tag{2.8}$$

In Eq. (2.8), ε is permittivity and μ is magnetic permeability. In order to perform the numerical solution of time-dependent Maxwell's equations, Yee developed a discretization scheme known as the Yee lattice. According to this scheme, six electromagnetic field components are placed at different points inside a cube called a cell or lattice. Yee introduced this scheme in 1966, which allows for the discretization of electromagnetic field components using the central difference method. The coordinates i, j, k in figure 4 represent cell coordinates. The components Ex, Ey, Ez, Hx, Hy, Hz shown in the figure represent the electric and magnetic field values in the i, j, k cell region.

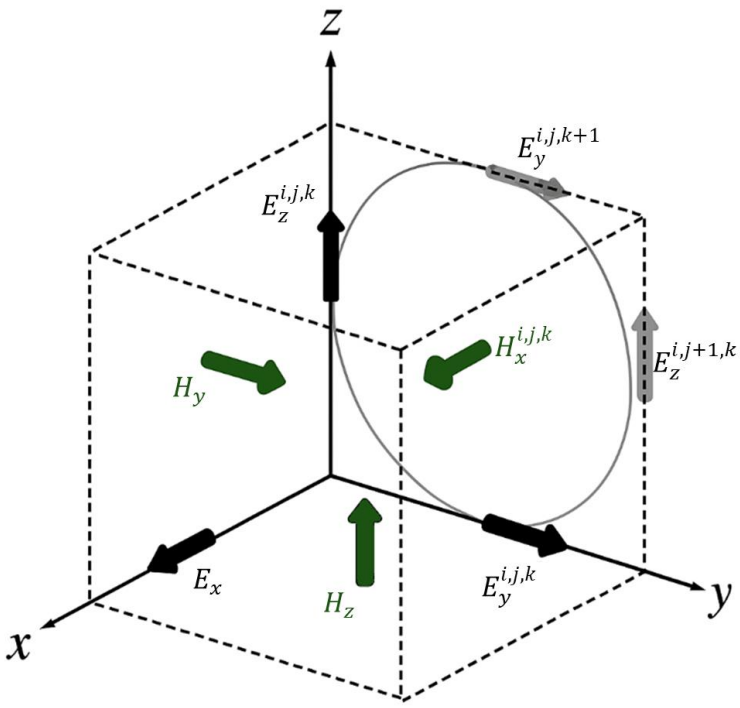

Figure 4. Yee lattice or Yee grid

Maxwell's curl equations can be rearranged by addition of constitutive relations.

$$\nabla x\vec{E} = -[\mu]\frac{\partial\vec{H}}{\partial t} \tag{2.9}$$

$$\nabla x\vec{\tilde{H}} = [\varepsilon]\frac{\partial\vec{E}}{\partial t} \tag{2.10}$$

Curl equations are vector equations and can be represented as three partial differential equations.

$$\frac{\partial E_z}{\partial y} - \frac{\partial E_y}{\partial z} = -\mu_{xx}\frac{\partial H_x}{\partial t} \tag{2.11}$$

$$\frac{\partial E_x}{\partial z} - \frac{\partial E_z}{\partial x} = -\mu_{yy}\frac{\partial H_y}{\partial t} \tag{2.12}$$

$$\frac{\partial E_y}{\partial x} - \frac{\partial E_x}{\partial y} = -\mu_{zz}\frac{\partial H_z}{\partial t} \tag{2.13}$$

$$\frac{\partial H_z}{\partial y} - \frac{\partial H_y}{\partial z} = \varepsilon_{xx}\frac{\partial E_x}{\partial t} \tag{2.14}$$

$$\frac{\partial H_x}{\partial z} - \frac{\partial H_z}{\partial x} = \varepsilon_{yy}\frac{\partial E_y}{\partial t} \tag{2.15}$$

$$\frac{\partial H_y}{\partial x} - \frac{\partial H_x}{\partial y} = \varepsilon_{zz}\frac{\partial E_z}{\partial t} \tag{2.16}$$

While writing the equations, it has been assumed that the material under consideration exhibits diagonal anisotropy, and non-diagonal terms in electric and magnetic permeabilities have not been included in the equations.

The first equation within the system of equations can be represented as follows through the utilization of the central difference method. This partial differential equation has been reformulated into an equation that incorporates central difference approximations for the two spatial derivatives of the electric field in the y and z coordinates, along with the time-dependent alteration of the magnetic field in the x-axis.

$$\frac{E_z^{i,j+1,k}\big|_t - E_z^{i,j,k}\big|_t}{\Delta y} - \frac{E_y^{i,j,k+1}\big|_t - E_y^{i,j,k}\big|_t}{\Delta z} = -\mu_{xx}^{i,j,k}\frac{H_x^{i,j,k}\big|_{t+\frac{\Delta t}{2}} - H_x^{i,j,k}\big|_{t-\frac{\Delta t}{2}}}{\Delta t} \tag{2.17}$$

To ensure numerical stability, it is imperative that each equation maintains consistent electric and magnetic field values at identical spatial points. On the left-hand side of the equation, a central difference approach using the electric field values of *(i, j, k)* and *(i, j+1, k)* cells (Fig. 4) can be observed for computing E_Z. The same applies to E_Y. This approach allows the acquisition of E_Z and E_Y values at the same location as H_Y. Similarly, on the right-hand side of the equation, a central difference approach is applied using the

magnetic field components at times t+Δt/2 and t-Δt/2. This enables the calculation of the magnetic field component at time t, which corresponds to the electric field component at the same moment on the left-hand side of the Eq. (2.17).

In certain systems, the geometry of the problem can be expressed in one dimension. For instance, in problems involving materials, geometries, and fields that repeat themselves in the x and y axes, the derivatives with respect to x and y become zero since there is no change along these axes. To avoid complex equation notations, it is beneficial to continue explaining the method's operation over a system that repeats itself in the x and y coordinates.

In software applications that employ the FDTD method, adjustments are made in discretized curl equations to examine the time-dependent changes of electromagnetic waves. An example of such an adjustment in a problem reduced to one dimension is provided below.

$$H_x^{i,j,k}\Big|_{t+\frac{\Delta t}{2}} = H_x^{i,j,k}\Big|_{t-\frac{\Delta t}{2}} - \frac{\Delta t}{\mu_{xx}} \times \frac{E_y^{i,j,k+1}\Big|_t - E_y^{i,j,k}\Big|_t}{\Delta z} \tag{2.18}$$

$$E_y^{i,j,k}\Big|_{t+\Delta t} = E_y^{i,j,k}\Big|_t + \frac{\Delta t}{\mu_{xx}} \times \frac{H_x^{i,j,k+1}\Big|_t - H_X^{i,j,k}\Big|_t}{\Delta z} \tag{2.19}$$

The equations (2.18) and (2.19) demonstrate that at successive points in time, they can be derived using the values at the previous point. For example, the value of H_X at t+Δt/2 can be derived from the value at the point t-Δt/2. Equations in this form are referred to as update equations.

A fundamental FDTD algorithm calculates electric and magnetic field values at successive time steps using these update equations. The fundamental loop of a simulation program utilizing FDTD follows the structure shown in figure 5. The main loop ensures calculations are carried out up to the desired time step. While updating the magnetic and electric field values using the update equations, the loops continue until results for all cells within the simulation domain are obtained. Once calculations for all spatial coordinates are completed for a time step, the simulation proceeds to the next time step.

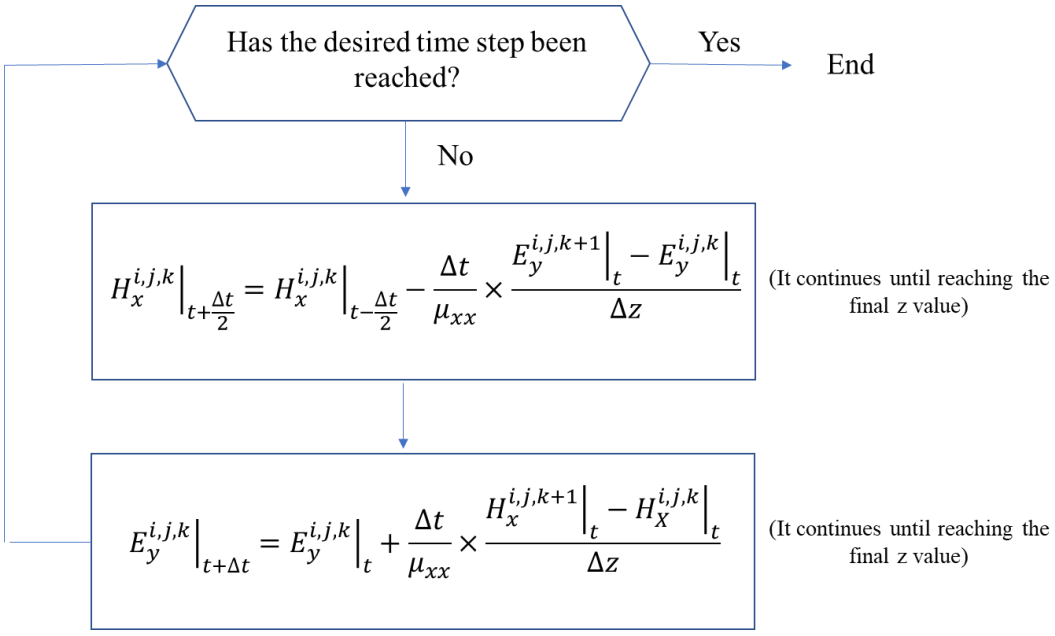

Figure 5. A fundamental FDTD algorithm

Each of the cells that divides the simulation domain has its own set of update equations. In other words, in the subsequent time steps, electric and magnetic field values are individually updated for each cell.

The simulation concludes when the desired time step is reached. Since results are recorded at successive time steps, changes in the electromagnetic field can be observed in the form of a video. Applying the Fourier transform to the time-dependent electromagnetic field functions, the solution can be transformed into the frequency domain. Using this method, the reflection, absorption, and transmission rates of radiation encountering different mediums can be easily calculated with a single simulation step.

In this section, a brief overview of the numerical solution of Maxwell's equations using the FDTD method has been provided. It should be noted that even in the simplest simulation tools, the algorithm contains far more steps than depicted in figure 5. The algorithms encompass grid resolution, normalizations employed to balance electric and magnetic field magnitudes, material and source properties within the simulation domain, initial and boundary conditions, boundary conditions updated within the loop, Fourier transforms, and code related to visualization. ANSYS Lumerical FDTD is utilized to perform numerical calculations in this study.

2.3 Design Methods

To achieve strong reflectance in MWIR band, first, a traditional design approach was employed. Geometric thicknesses of the dielectrics were calculated by choosing 4 μm as design wavelength. Analytical and numerical results were obtained and compared. Spectral reflectance with respect to number of layers was investigated. Second, Tandem Approach was applied using FDTD. MWIR band was divided into two parts and 3.5 and 4.5 μm were chosen as design wavelengths. Reflectance spectrums of designs addressing 3.5 and 4.5 μm were investigated separately. Then, these structures were placed on top of each other and reflectance spectrums of two different layered mediums were calculated. Finally, impedance mismatch based optimization were performed. Impedance mismatch based optimization is a physical based optimization method which aims equalizing the absolute value of complex reflectivity to unity. Reflectivity has real and imaginary parts. In complex plane, maximum reflectance points of a medium forms a circle. Optimization tool that is used in this study aims placing individual reflectivity points of different wavelengths on this circle by investigating varying layer thicknesses, therefore, maximizes the reflectance. Average reflectance's for all three approaches were calculated and widths of the high reflectance regions were discussed.

2.3.1 Quarter Wavelength Approach

To understand the quarter wavelength approach, it will be useful to examine the basic phenomenon called thin film interference. In this section, references (Cutnell & Johnson, 2009) and (Al-Azzawi, 2018) were used.

Upon the incidence of electromagnetic waves at an interface with a medium possessing a refractive index greater to that of the incumbent medium, the reflected wave experiences a phase shift of 180 degrees. Conversely, if the waves reflect from an interface between a medium whose refractive index is smaller to that of the prevailing medium, no phase shift is manifested in the reflected wave.

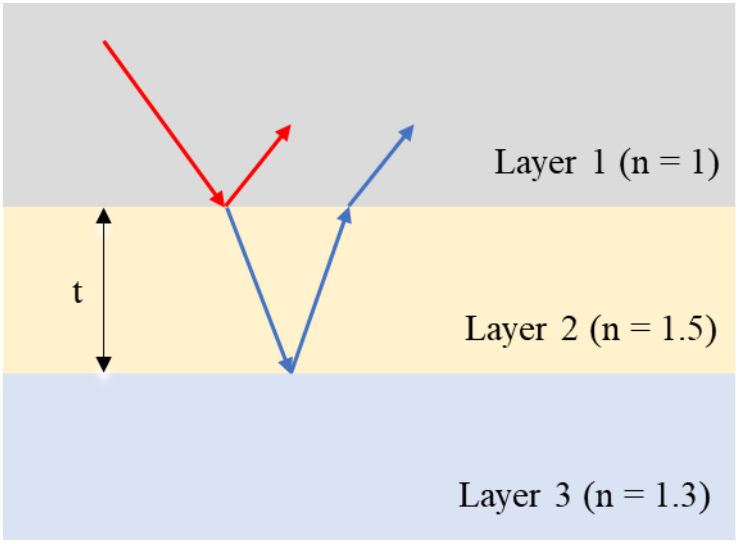

Figure 6. Light reflecting from different interfaces in a layered medium

Let's consider that the light travels between layers with refractive indices of 1, 1.5 and 1.3, respectively, as shown in figure 6. Upon reflection at the interface between layer 1 and layer 2, light undergoes a phase shift of 180 degrees, a phenomenon which is analytically equivalent to the propagation of the wave over a distance of half a wavelength (1/2λ). Within such a structure, the optical path length for light reflected at the interface between layer 2 and layer 3 extends by an additional distance equivalent to twice the thickness of layer 2 (2t), when compared with the path length for light reflected from the interface between layer 1 and layer 2.

In the presented scenario, the phase of wave 2 within the structure can be modulated by varying the thickness of layer 2. A phase discrepancy of 180 degrees between the waves results in them being out of phase, a condition known as destructive interference, wherein the waves effectively attenuate each other. Conversely, when the phases of the waves align, they are said to be in phase, leading to constructive interference. This alignment enhances the reflective properties of the structure. In order for the waves to be in phase, a minimum wavelength distance of 1/2 lambda must be covered at a distance of 2t. Similarly, traveling a distance of 3/2 or 5/2 lambda will also cause constructive interference. This principle can be expressed through the following formulation:

$$2t = \frac{1}{2}\lambda_{film}, \frac{3}{2}\lambda_{film}, \frac{5}{2}\lambda_{film}, \dots \dots \tag{2.20}$$

By including the refractive index of the film in the formula, the following adjustment can be made.

$$2t = \frac{1}{2}\frac{\lambda}{n}, \frac{3}{2}\frac{\lambda}{n}, \frac{5}{2}\frac{\lambda}{n}, \dots \dots \tag{2.21}$$

$$2t = \left(0 + \frac{1}{2}\right)\frac{\lambda}{n_{film}}, \left(1 + \frac{1}{2}\right)\frac{\lambda}{n_{film}}, \left(2 + \frac{1}{2}\right)\frac{\lambda}{n_{film}}, \dots \dots \tag{2.22}$$

$$2t = \left(m + \frac{1}{2}\right)\frac{\lambda}{n_{film}}, (m = 0, 1, 2, \dots) \tag{2.23}$$

The principle of thin film interference has facilitated the emergence of diverse applications. In the construction of anti-reflective coatings, the layering is applied to create destructive interference. Conversely, Bragg reflectors are engineered by calibrating the layer thicknesses to λ/4n, in alignment with Eq. (2.23), thereby crafting highly reflective architectures. Constructive interference can be represented as in figure 7. This methodology allows obtaining structures that exhibit significant reflection at the target wavelength.

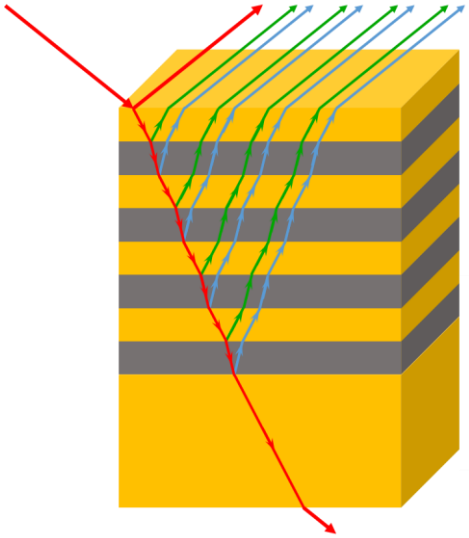

Figure 7. Representation of constructive interference in a DBR

Within the scope of the study, reflective structures were developed using the quarter-wavelength approach by selecting the design wavelength of 4 µm, which is the middle of MWIR.

2.3.2 Tandem Approach

This section is inspired by the tandem approach, which combines designs for different spectral regions. It is frequently used to increase the efficiency of solar panels (Razi et al., 2023; Jäger et al., 2021). In the tandem approach, the MWIR band was divided into two and two different DBR structures with design wavelengths of 3.5 and 4.5 microns were developed. By placing the buildings on top of each other, it was aimed to expand the area where high reflectance could be achieved and to increase the average reflectance. The spectral areas targeted in separate designs are colored blue (3-4 µm) and orange (4-5 µm) in figure 8.

Two different structure were designed to cover 3-4 µm and 4-5 µm ranges separately

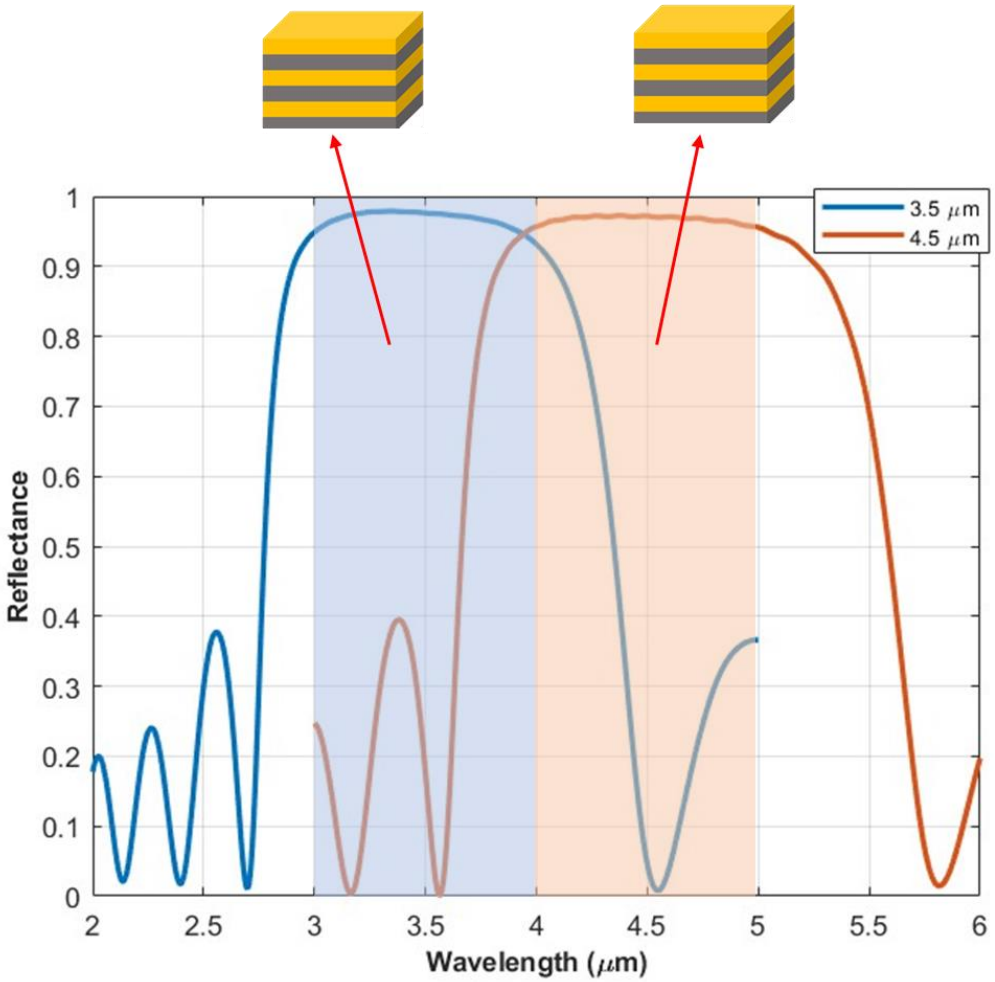

Figure 8. Dividing MWIR band and aiming high reflectance with two different layered mediums

2.3.3 Impedance Mismatch Based Optimization

The impedance matching method is a technique employed to maximize energy transfer in transmission lines (Balabanian, 1955). The primary objective of this method is to minimize losses between the source and the load in various electronic systems (De Piante & Tonello, 2016; Weiwei, 2012). The loss reduction approach, which relies on impedance matching in transmission lines, is also applicable to optical designs (Keçebaş, 2020). In this context, the intrinsic impedances of the media between the environment and the substrate are adjusted to optimize optical transmittance. When the properties of the intermediate media are appropriately tailored, the structure's transmittance can be minimized, and high reflectance can be achieved (Koucheh et al., 2021).

The reflectivity of a multilayer thin-film structure can be determined based on the impedance of the structure. The impedance of a single layer is calculated using its material properties, as outlined in Eq. (2.24).

$$Z = \sqrt{\frac{\mu}{\varepsilon}} \tag{2.24}$$

where μ is magnetic permeability and ε is dielectric permittivity. The impedance at the surface of a multilayer film structure can be determined using the impedances of the individual layers, their optical thicknesses, and the surface impedances of the layers, as described in Eq. (2.25).

$$\not{Z}_i = Z_i \frac{\not{Z}_{i+1} + Z_i \tan(\delta_i)}{Z_i + j\not{Z}_{i+1} \tan(\delta_i)} \tag{2.25}$$

Reflection coefficient can be derived using the surface impedance of the layered thin film structure and the impedance of the medium as follows.

$$\Gamma = \frac{Z_1/Z_0 - 1}{Z_1/Z_0 + 1} \tag{2.26}$$

The reflectivity of the structure can be calculated using the reflectivity coefficient with the following relation.

$$R(\lambda) = |\Gamma(\lambda)|^2 \tag{2.27}$$

The reflection coefficient is a complex quantity. The reflection coefficients obtained at different wavelengths are represented in the complex impedance plane, as shown in Figure 9. The red point in the figure denotes the ideal impedance matching point. When the reflection coefficients for wavelengths within the 3–5 μm range are located near the red point, the transmittivity of the layered thin-film structure is high. Conversely, when the coefficients lie on the blue circle with a radius of 1, the reflectivity of the structure increases.

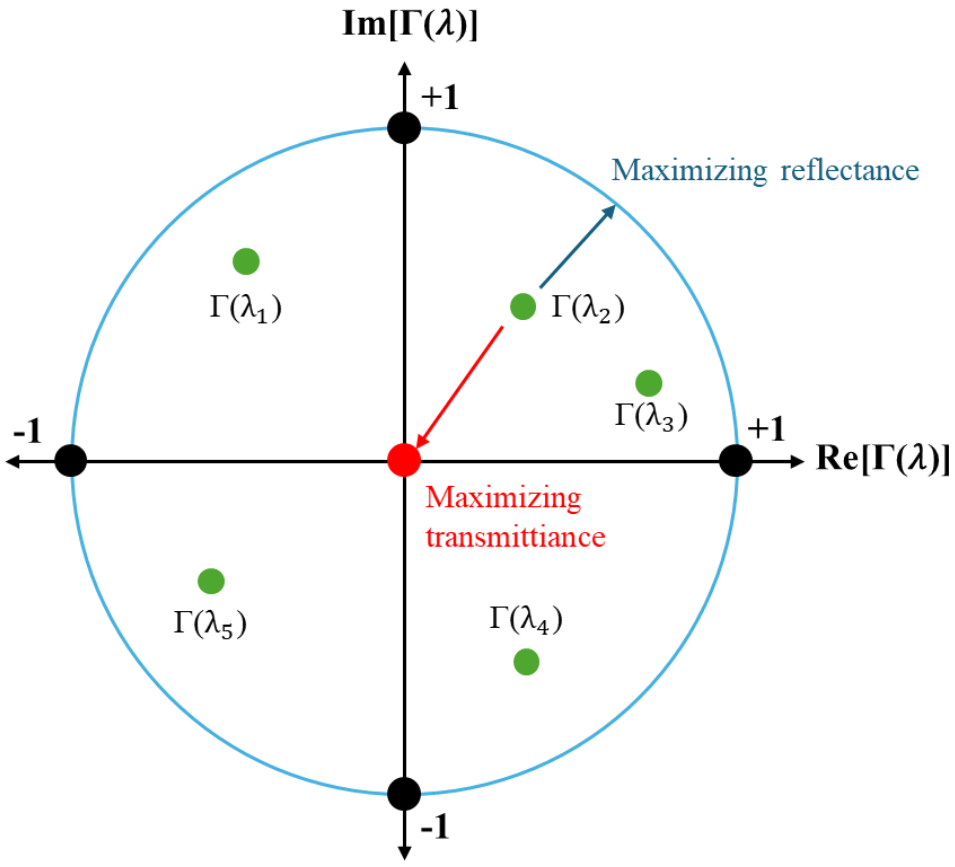

Figure 9. Reflectance coefficient in complex impedance plane

The optimization method works to maximize the reflectivity by appropriately adjusting the thickness of the individual layers and bringing the reflectivity coefficient values closer to blue circle for each wavelength.

2.4 Results

2.4.1 Quarter-Wavelength Approach

Around the center frequency of 4 μm (center of the band), thicknesses were calculated using quarter wavelength approach. The effect of number of layers was investigated by simulating the structure with 2, 4, 6, 8, 10- and 12-layered coatings.
Numerical results that were obtained by FDTD and analytical results that were obtained by TMM were given in figure 10 and 11 respectively.

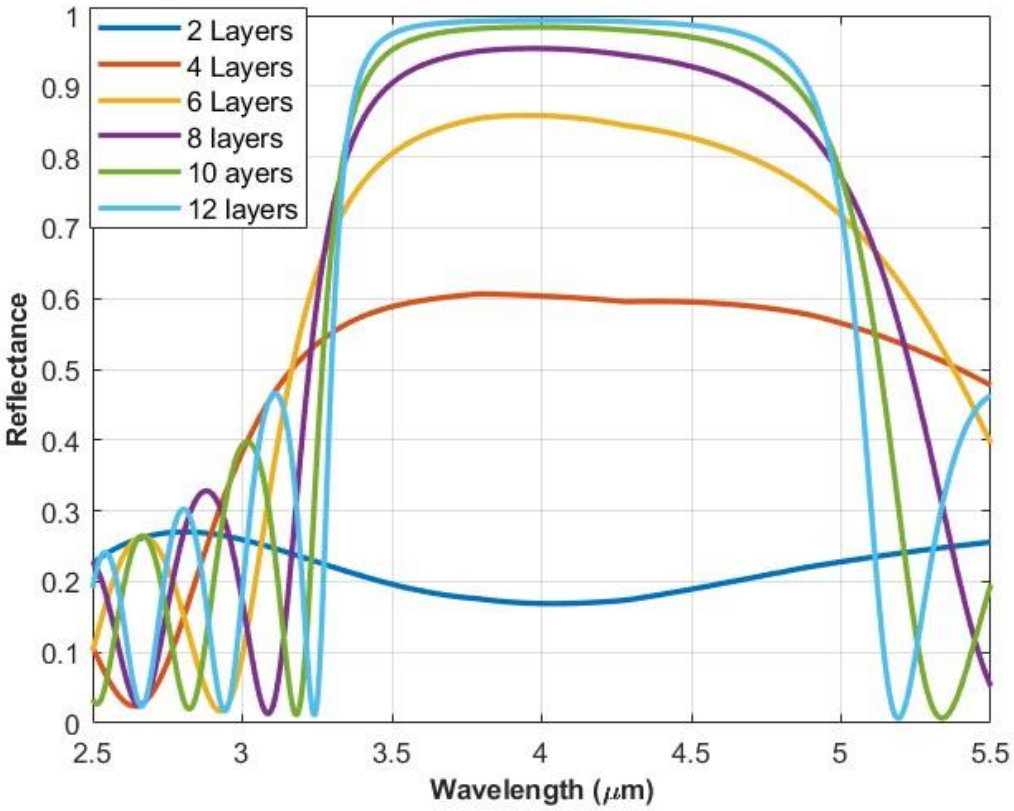

Figure 10. Reflectance spectrum of 2, 4, 6, 8, 10 and 12-layered coatings obtained by TMM.

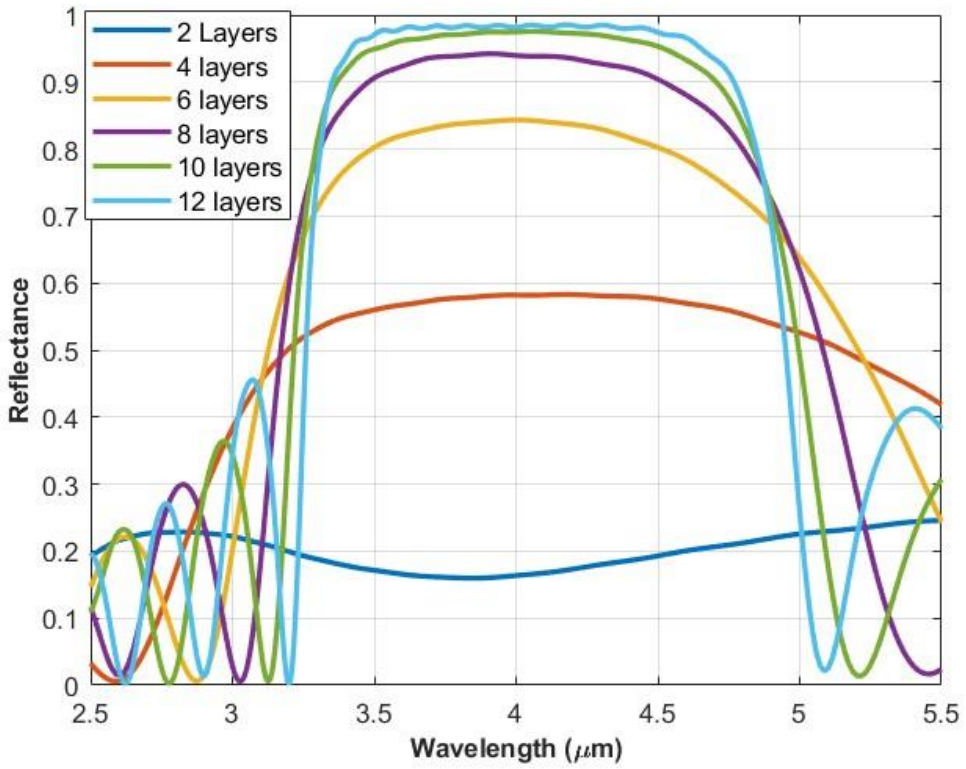

Figure 11. Reflectance spectrum of 2, 4, 6, 8, 10 and 12-layered coatings obtained by Lumerical.

According to figures numerical and analytical results are firmly consistent and both indicate that spectral reflectance can be enhanced by increasing the number of layers. This enhancement is predictable since the greater number of layers the more interfaces for reflection. As seen, reflectance of layered structure increases to 10-layer significantly. Results of 10- and 12-layered structures are nearly same. Therefore, 10-layered structure can be counted as adequate for sufficient reflectivity.

Table 2. Average reflectance of SiO2 and varying number of layers

Sample	**Average Reflectance (TMM)**	**Average Reflectance (FDTD)**
SiO_2	0.03	0.02
2-Layered Structure	0.20	0.18
4-Layered Structure	0.57	0.54
6-Layered Structure	0.76	0.73
8-Layered Structure	0.81	0.77
10-Layered Structure	0.85	0.79
12-Layered Structure	0.86	0.80

Reflectance spectrum of 10-layered structure that was obtained by both FDTD and TMM and pristine substrate are given in figure 12. Average reflectance of 10-layered structure and SiO_2 are given in table 2. SiO_2 is transparent in 3-5 μm band and its average reflectance was calculated about 0.02. Average reflectance of 10-layered 4 μm structure was calculated about 0.79, approximately 45 times the that of SiO_2. This indicate that a transparent surface can be transformed to highly reflective one with 10-layered structure.

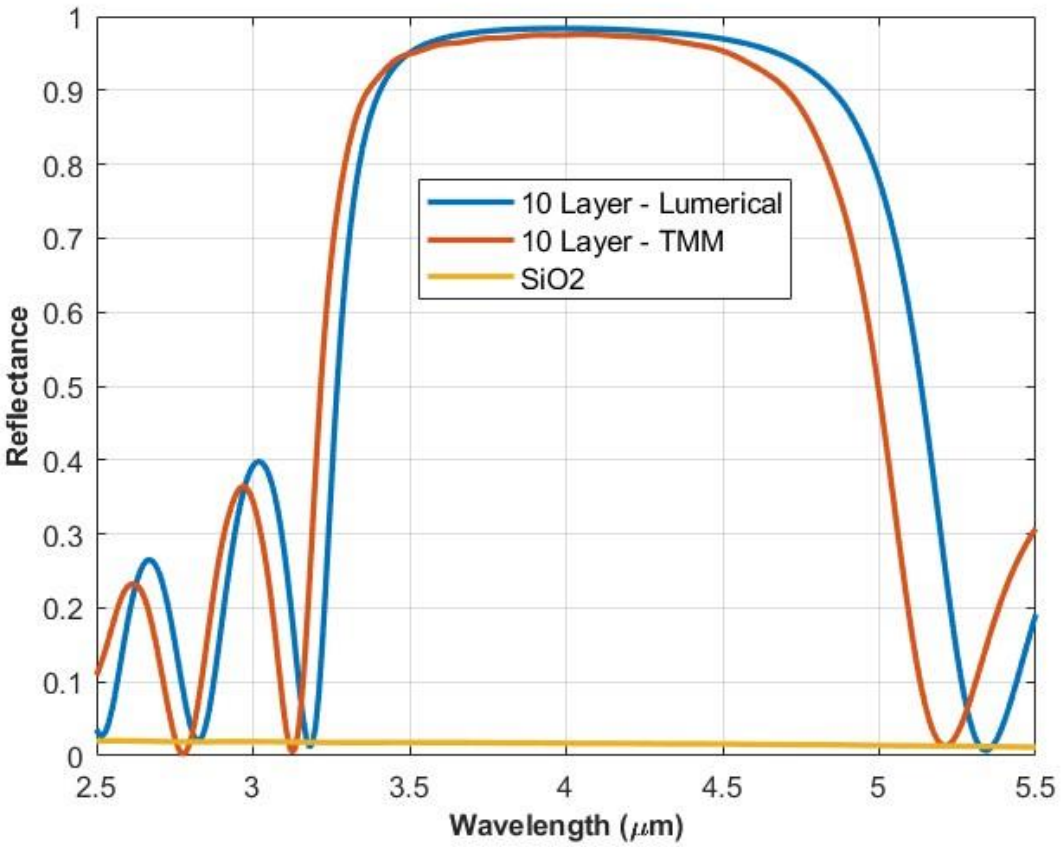

Figure 12. Reflectance spectrum of substrate 10-layered structure obtained by TMM and Lumerical.

Although high reflectivity enhancement was achieved reflectance is low at wavelengths close to 3 µm. To increase average reflectance and obtain high reflectance across 3-5 µm band, further studies were conducted.

It has been observed that thickness variation can typically be limited to just a few nanometers across all thin-film production methods. Relevant studies are discussed under the heading Future Works and Limitations. To evaluate the impact of such thickness variations on reflectivity, simulations were conducted and compared with results obtained using ideal layer thicknesses. To model a worst-case scenario, the thickness of the TiO_2 films in the stack was reduced by 5 nm, while the thickness of the SiO_2 layers was increased by 5 nm. The results showed that, at the design wavelength center (MWIR), reflectivity remained similar to that of the ideal structure. However, it was also observed that the average reflectivity slightly decreased as the number of layers increased.

Table 3. Comparison of reflectivity values obtained with ideal and error-added thicknesses.

Sample	**Average Reflectance Obtained with λ/4n Thicknesses**	**Average Reflectance for Sensitivity Analysis**
2-Layered Structure	0.20	0.18
4-Layered Structure	0.57	0.54
6-Layered Structure	0.76	0.72
8-Layered Structure	0.81	0.76
10-Layered Structure	0.85	0.75
12-Layered Structure	0.86	0.77

2.4.2 Tandem Approach

Tandem approach was applied. 3-5 μm band was divided and two different structures were designed. Around the center frequency of 3.5 μm and 4.5 μm, thicknesses of dielectrics were calculated using Eq. (2.23). Reflectance spectrum of 10-layered 3.5 μm and 4.5 μm-structures are given in figure 13. FDTD was used since reliability is verified.

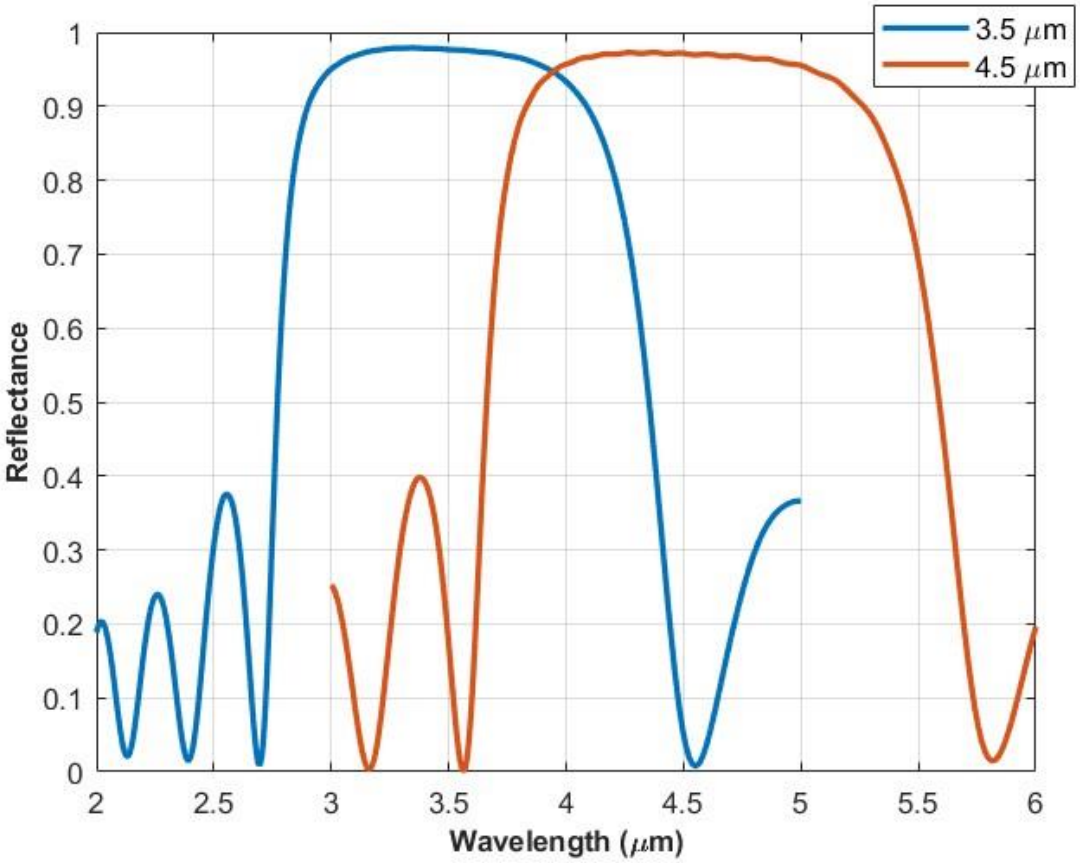

Figure 13. Reflectance spectrum of 10-layered structures that is designed addressing 3.5 µm and 4.5 µm.

As seen, 10-layered 3.5 µm design cover wavelengths close to 3 µm and 10-layered 4.5 µm design cover wavelengths close to 5 µm. These structures were placed on top of each other and simulations were run. Design was named as Tandem-3.5 µm when 10-layered-3.5 µm structure is on top of 10-layered-4.5 µm. Reflectance spectrums of Tandem – 3.5 µm and Tandem 4.5 µm are given in figure 14. As seen, response of structures are similar to each other.

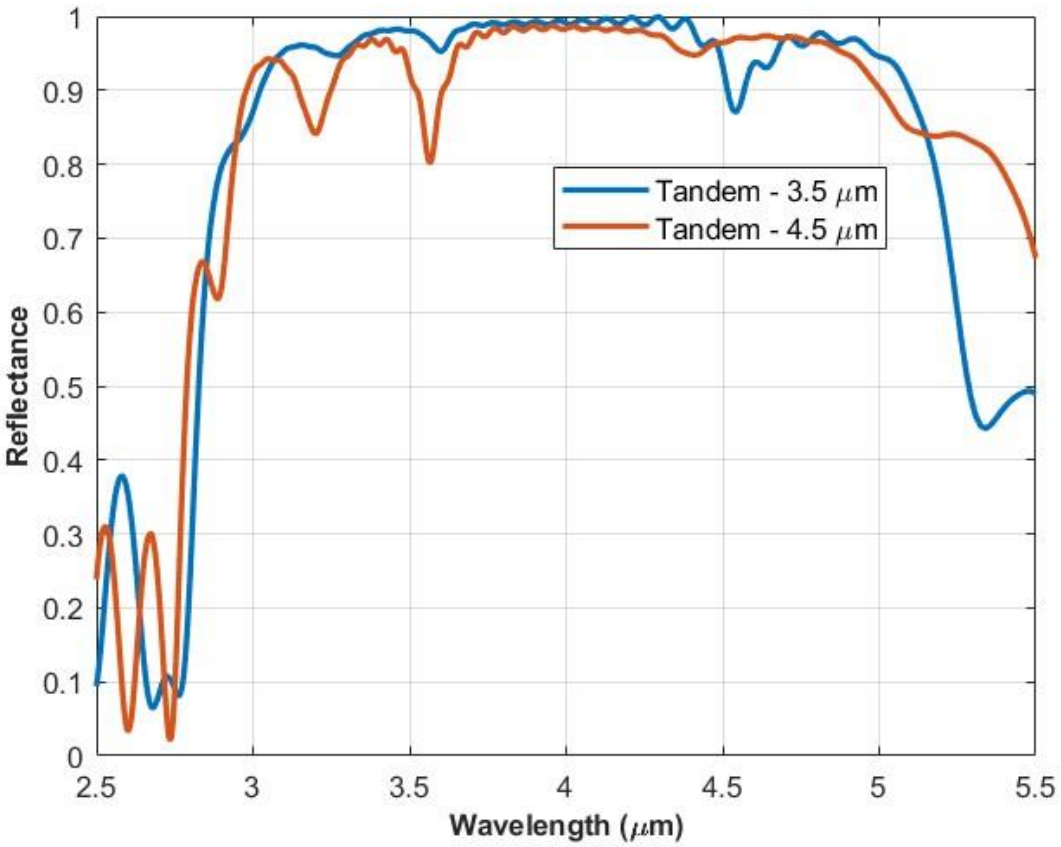

Figure 14. Reflectance spectrum of Tandem - 3.5 um and Tandem 4.5 um

Reflectance spectrum and average reflectance of tandem structures 10-layered 4 μm design and pristine substrate are given in figure 15 and table 4 respectively.

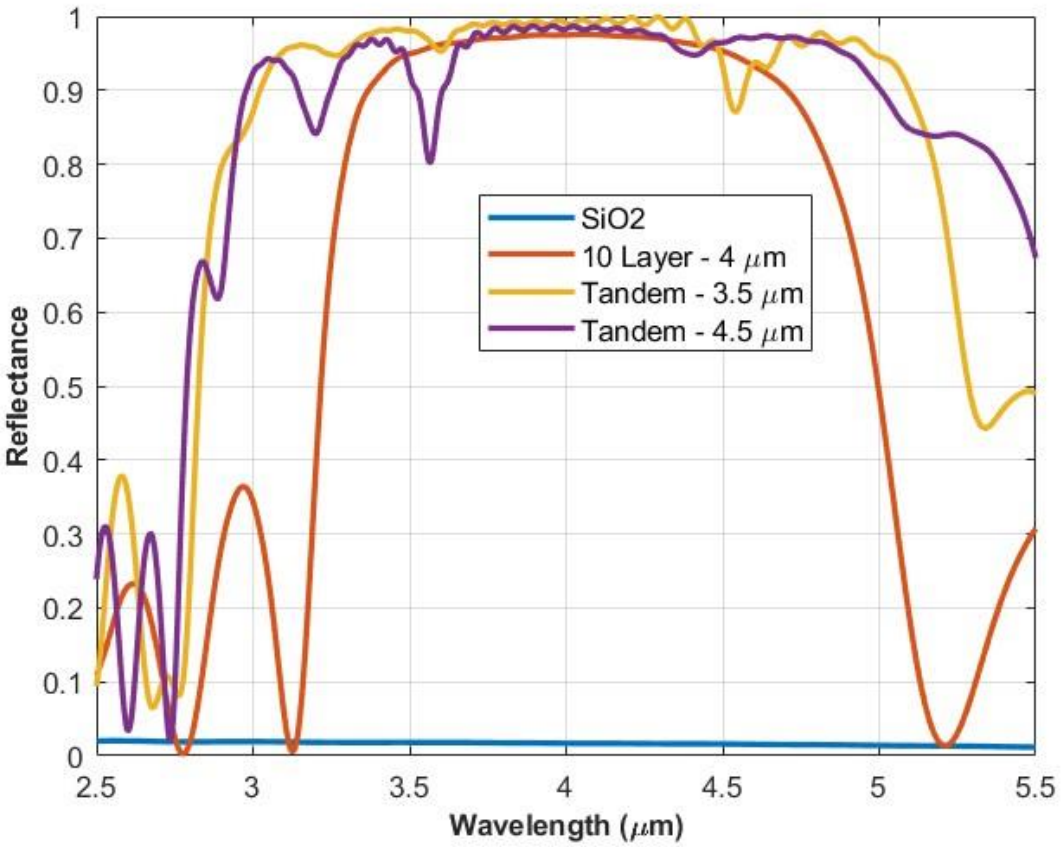

Figure 15. Reflectance spectrum of SiO_2, 10-layered structure, Tandem-3.5 µm and Tandem-4.5 µm

Table 4. Average reflectance of SiO2, 10-layered structure, Tandem-3.5 µm and Tandem-4.5 µm

Sample	**Average Reflectance**
SiO_2	0.02
10-Layered Structure	0.79
Tandem – 3.5 µm	0.97
Tandem – 4.5 µm	0.95

As seen in figure 15, tandem structures provide wider high reflectivity region than simple 4 µm design. Average reflectance of Tandem-3.5 µm is a slightly more than that of Tandem-4.5 µm, approximately 56 times the that of SiO_2. This also indicates that when radiation coming from sun encounters with a structure addressing wavelengths close to UV first, more reflection occurs.

2.4.3 Impedance Mismatch Based Optimization

Impedance Mismatch based optimization was applied in 3-5 μm band to see if efficiency of the design can be enhanced using heterogeneous thicknesses of the dielectrics. When optimization was run with 10 layers, it was seen that the thickness of the top layer was calculated very close to 0. So that, optimization-based design studies continued with 9-layers. Some of the thicknesses and average reflectance levels that was obtained by optimization were given in Table 5.

Table 5. Thicknesses and average reflectance of two different data sets obtained using Impedance Mismatch Based Optimization

Thickness (9-layers)	512	370
	761	671
	381	367
	672	671
	364	369
	649	670
	341	746
	1554	668
	337	371
Average Reflectance	0.92	0.93

To confirm optimization studies, thicknesses in Table 5 were used in the Lumerical and results in figure 16 were obtained.

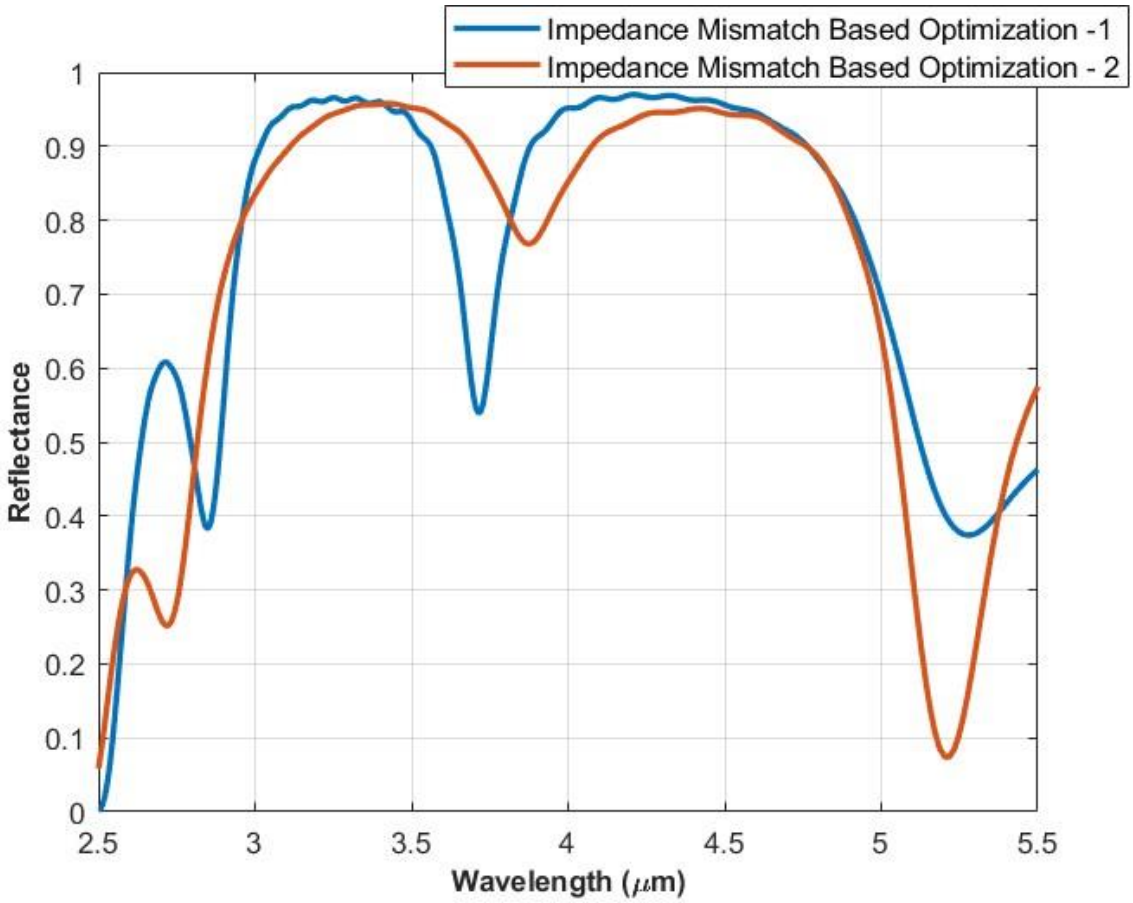

Figure 16. Reflectance spectrum of 9-layered structures with different thickness configurations that is obtained by Impedance Mismatch Based Optimization

As seen in figure 16, strong reflectance can be achieved across MWIR band with different thicknesses. Average reflectance was calculated as 0.90 for both thickness configurations. Differences between the average reflectance of optimization tool and Lumerical is approximately 0.02 and 0.03 for first and second thickness configuration respectively. The differences arise due to the disparity between numerical and analytical methods employed in the study. On the other hand, optimization method provides 15% higher average reflectance than that of traditional approach with similar number of layers. Also, it is observed that average reflectance higher than 90% can be obtained using both Tandem approach with 20 layers and Impedance Mismatch based Optimization with 9 layers. Therefore, to achieve strong reflectance in an efficient way optimization can be performed.

3. LWIR

3.1 Problem Definition

Mid-wave infrared (MWIR) research, modeling and design methodologies have been extended to long wave infrared (LWIR). However, this transition has encountered challenges, particularly with materials such as titanium dioxide (TiO_2) and silicon dioxide (SiO_2), which, despite their efficiency in MWIR applications, have not yielded the anticipated outcomes when employed in LWIR studies. As seen in figure 17, in the 3-5 μm band, these materials exhibit nearly constant refractive index differences across the band, with extinction coefficients approaching zero. In contrast, within the 8-12 μm band, the refractive index disparity of these same materials undergoes dramatic variations. Specifically, extinction coefficient of SiO_2 has a peak around 9 μm, whereas extinction coefficient of TiO_2 exhibits a notable increase after 10 μm. Consequently, this evidences a substantial divergence in the optical properties of these materials between the 3-5 and 8-12 μm bands.

In light of these findings, a thorough investigation into alternative materials compatible with the 8-12 μm band for similar modeling and design purposes was undertaken. This exploration identified MgF_2 Magnesium Fluoride (MgF_2) and Zinc Sulfide (ZnS) as potential candidates, attributed to their near-zero extinction coefficients and consistent refractive index differences throughout the 8-12 μm band. Accordingly, it was concluded to adopt ZnS as the high index material and MgF_2 as the low index material.

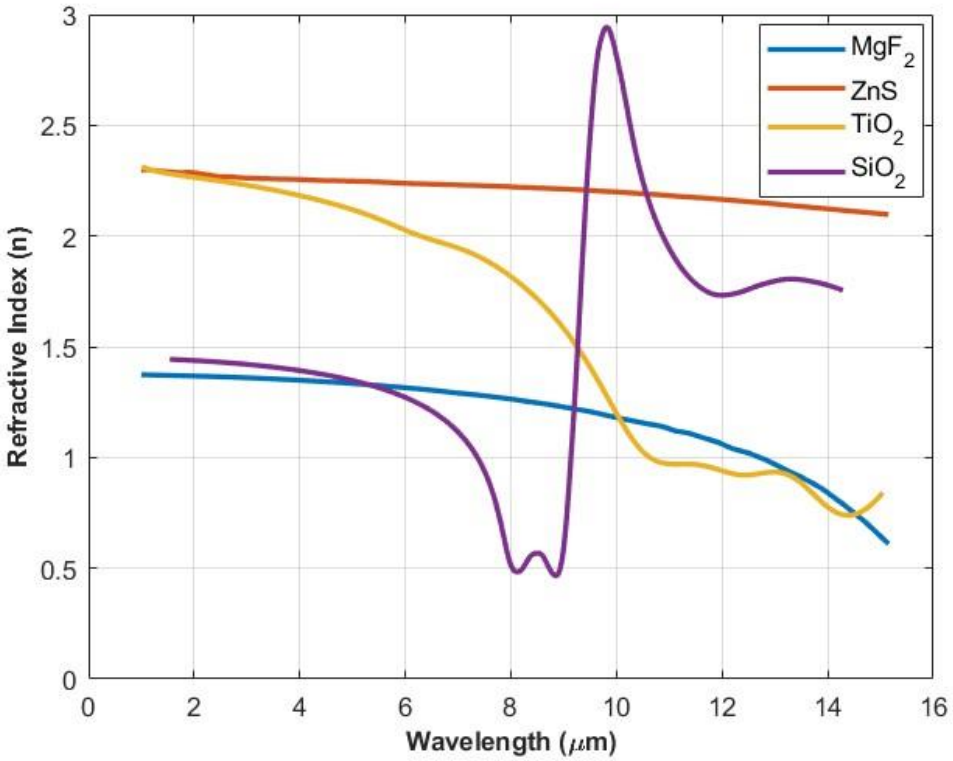

Figure 17. Refractive indices of materials

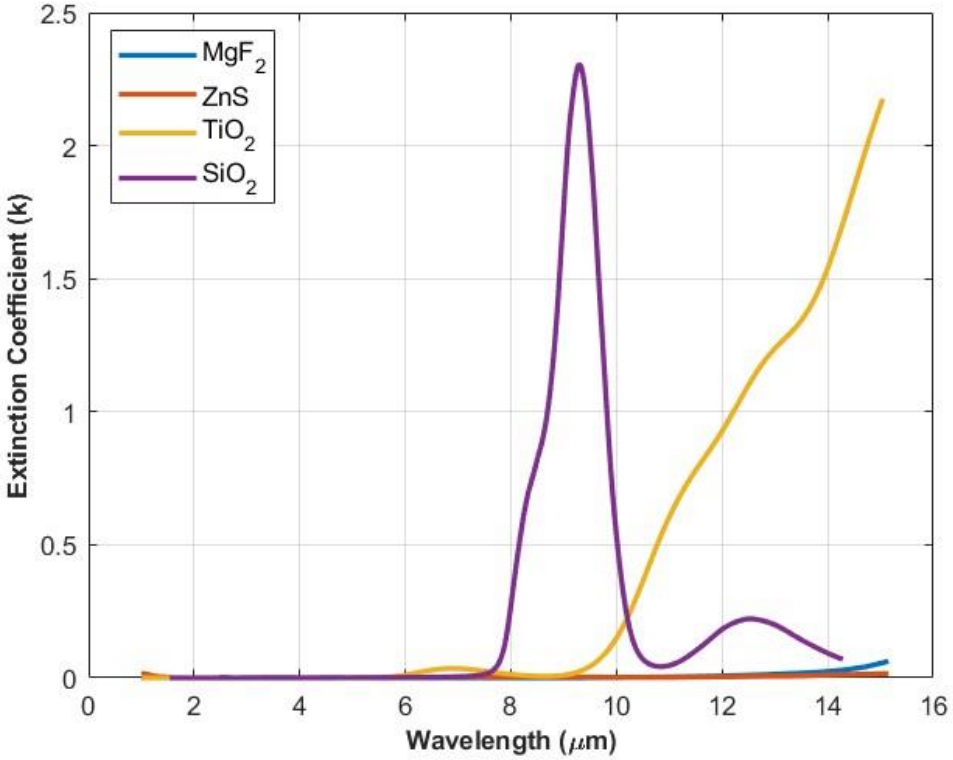

Figure 18. Extinction coefficients of materials

In this section, the methods employed in MWIR and LWIR studies were applied to achieve broadband selective reflectivity. The feasibility and effectiveness of these methods for this purpose were analyzed.

The ideal spectral behavior of a selectively reflective filter operating in the MWIR and LWIR bands is as shown in figure 29. It should provide maximum reflectivity between 3-5 µm and 8-12 µm and minimum reflectivity in the other bands.

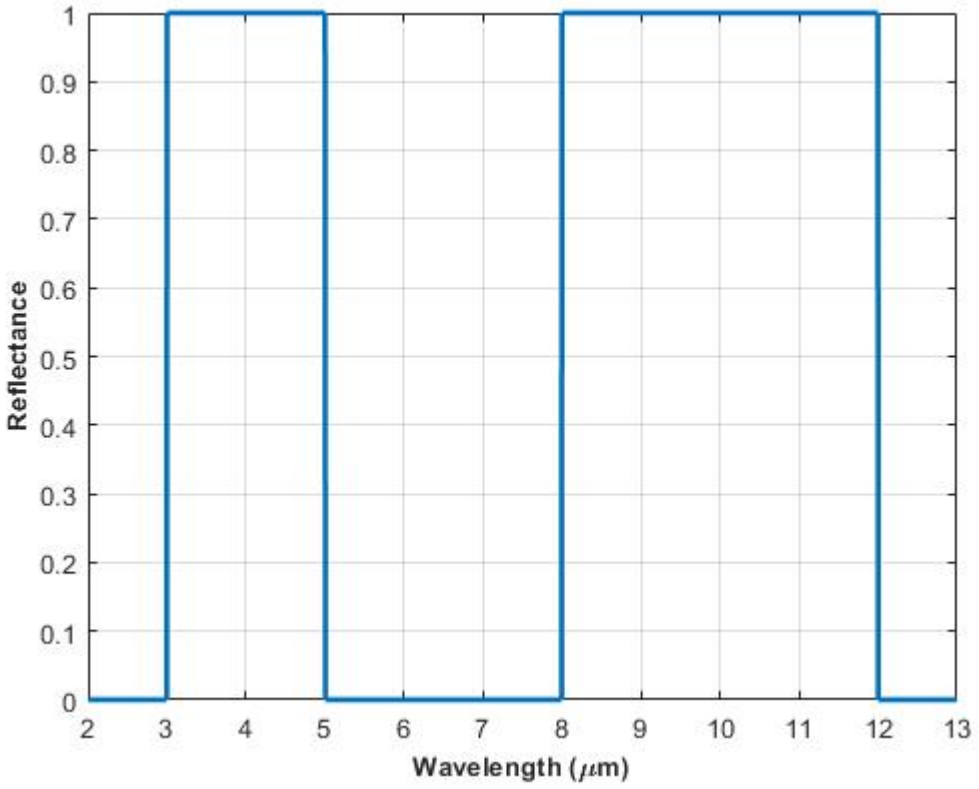

Figure 19. Reflectance spectrum of ideal spectrally selective multiband filter

First, broadband performance of multilayer structure that is designed for LWIR calculated. Then, the impedance mismatch-based optimization method is applied. Considering that their optical properties are more suitable for broadband operation, MgF_2 and ZnS are used. The performance of the MgF_2/ZnS thin films developed with impedance mismatch-based optimization was compared with the broadband performance of the structure designed for the LWIR band.

3.2 Results

3.2.1 Quarter-Wavelength Approach

Using the quarter wavelength approach at a central wavelength of 10 μm, the thicknesses of the materials have been calculated. In calculations employing the traditional approach, the thicknesses of MgF_2 and ZnS have been utilized as 2119 and 1137 nanometers, respectively.

Numerical results that were obtained by FDTD and analytical results that were obtained by TMM were given in figure 20 and 21 respectively.

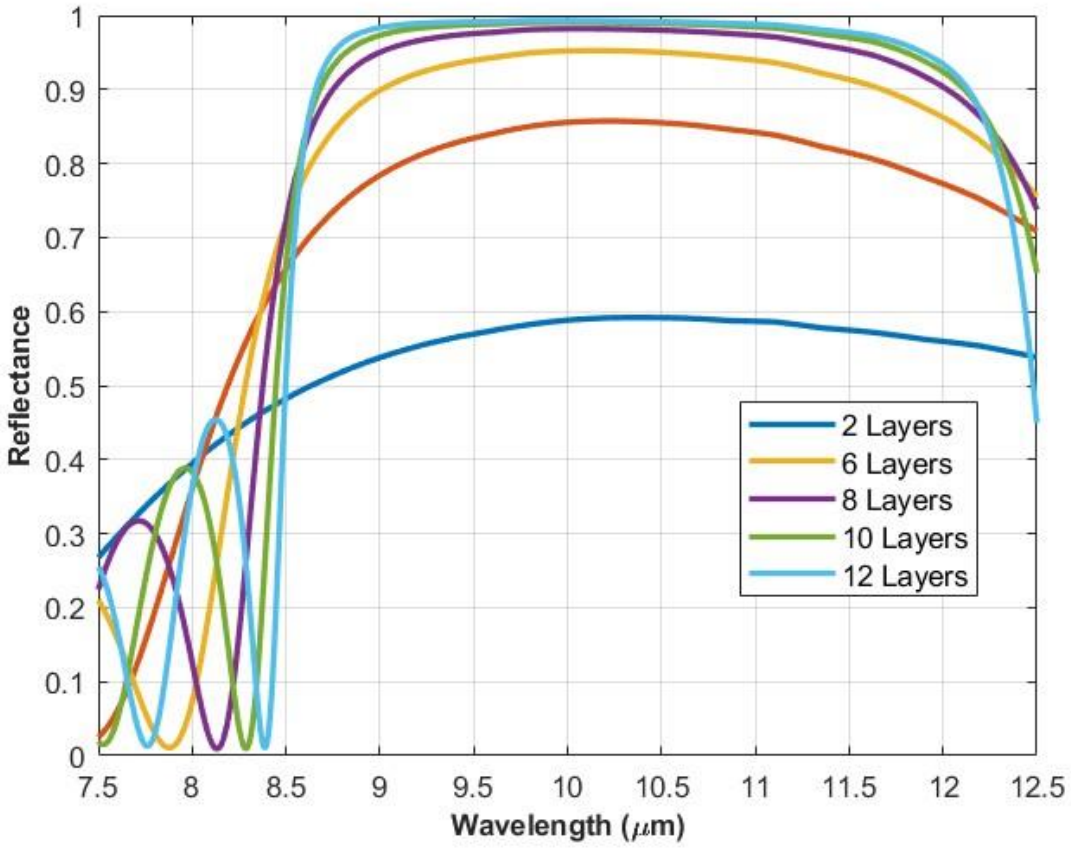

Figure 20. Reflectance spectrum of 2, 4, 6, 8, 10 and 12-layered coatings obtained by TMM.

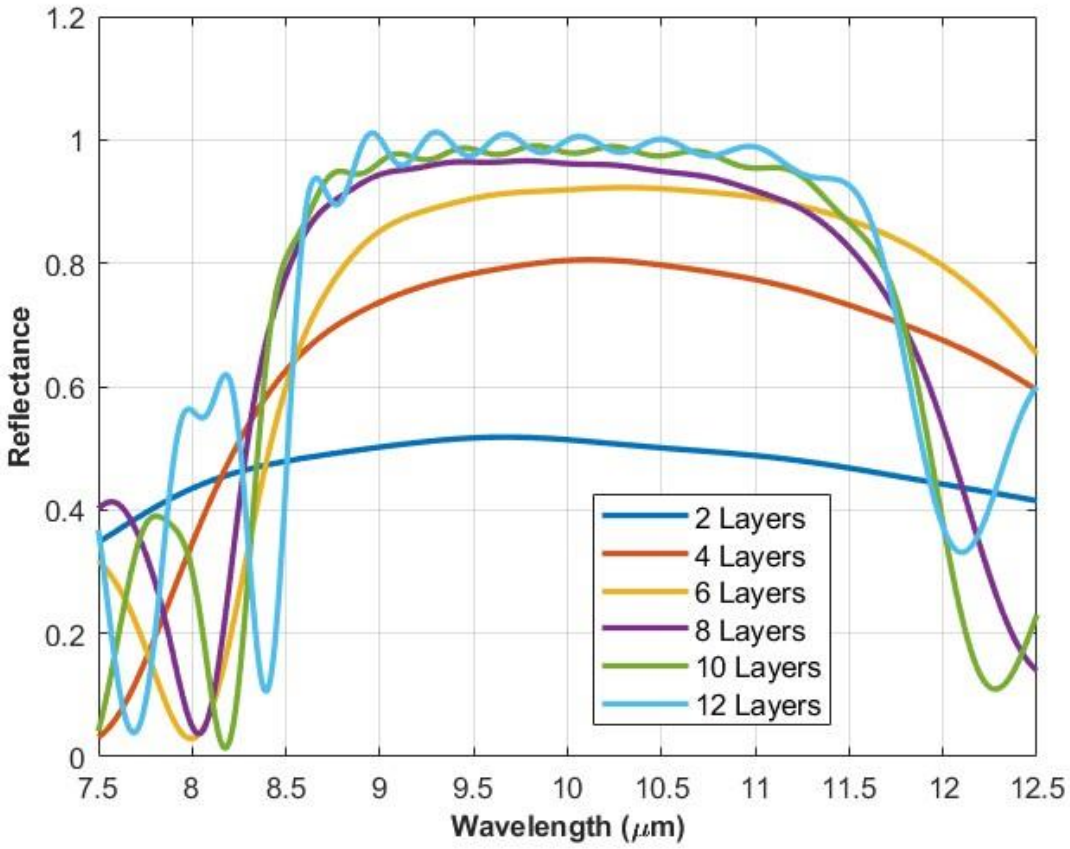

Figure 21. Reflectance spectrum of 2, 4, 6, 8, 10 and 12-layered coatings obtained by FDTD.

As seen in figure 20 and 21, analytical and numerical results are consistent. On the other hand, In the numerical results, ripples were formed as the number of layers increased which indicates that analytical method is more reliable for modelling in LWIR. Therefore, the studies were continued with TMM, which is an analytical modeling and analysis method. (Onur: 12 Layer FDTD sonuçlarında problem var. Bu sonuçlara tekrar bakabilir misin?)

According to the results in the figures and table 6 as the number of layers increases, the reflectance enhances. Considering the analytical results, 0.88 of reflectance was obtained with 10 layers. This shows that Quarter-Wavelength Approach works better in LWIR band than that of MWIR.

Table 6. Average reflectance and thickness of ZnS and varying number of layers

Sample	Average Reflectance (TMM)	Average Reflectance (FDTD)	Total Thickness of Layers (nm)
ZnS	0.14	0.10	-
2-Layered Structure	0.55	0.49	3256
4-Layered Structure	0.78	0.71	6512
6-Layered Structure	0.85	0.76	9768
8-Layered Structure	0.87	0.81	13024
10-Layered Structure	0.88	0.82	16280
12-Layered Structure	0.89	0.84	19536

3.2.2 Tandem Approach

Although, Quarter-Wavelength Approach works well in LWIR, the Tandem Approach was implemented to enhance the reflectance and expand the region where high reflectance is achieved. Reflectance spectrum of DBRs designed by Tandem approach with varying number of layers are given in figure 22. Additionally, the average reflectance of stacks are given table 7.

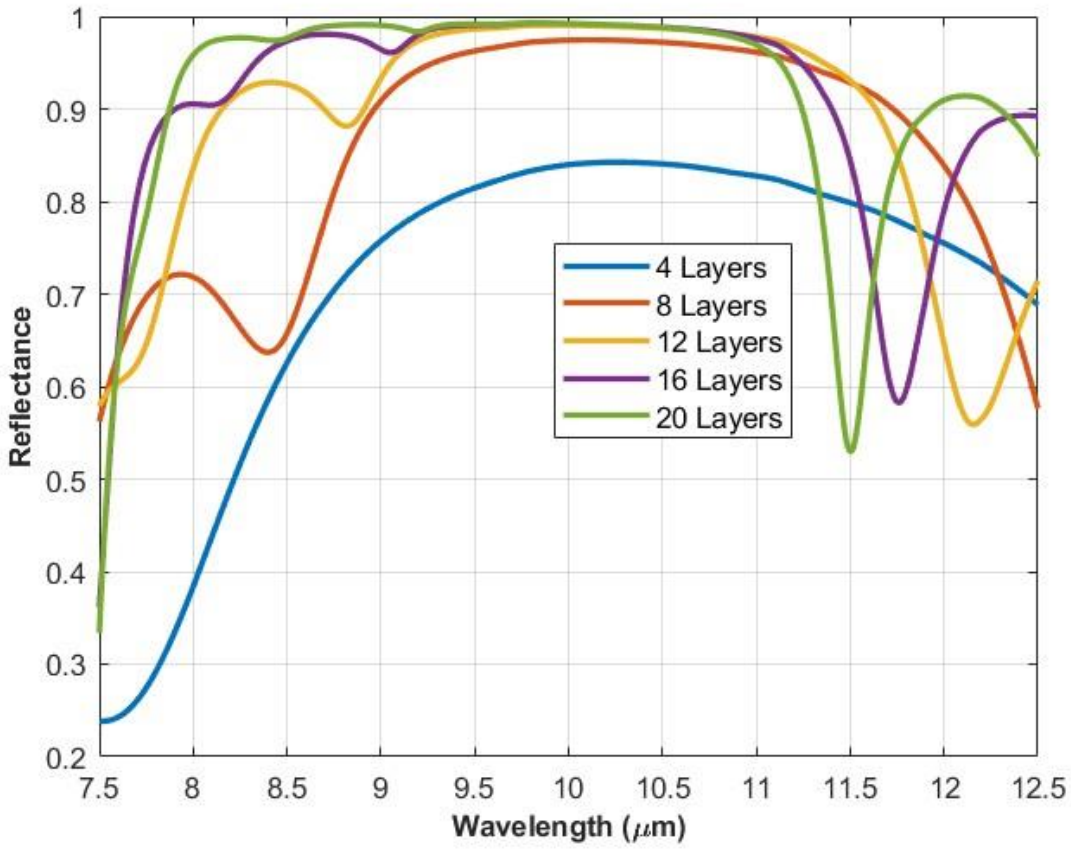

Figure 22. Reflectance spectrum of 4, 8, 12, 16, 20-layered coatings designed by Tandem Approach

Table 7. Average reflectance of Tandem structures with varying number of layers

Sample	**Average Reflectance**	**Total Thickness of Layers (nm)**
4-Layered Structure	0.762387	6547
8-Layered Structure	0.895211	13094
12-Layered Structure	0.941292	19641
16-Layered Structure	0.935232	26188
20-Layered Structure	0.942764	32735

The results indicate that the Tandem Approach can yield higher reflectivity compared to the Quarter-Wavelength method when utilizing 8 layers. While an average reflectance of 0.89 was achievable with 12 layers through the Quarter-Wavelength method, the Tandem Approach attained this level with only eight layers. Employing 12 layers in the Tandem Approach resulted in a significantly high reflectance value of 0.94. A noteworthy

observation is that the performance enhancement does not persist beyond 12 layers within the Tandem Approach. Utilizing 16 and 20 layers produced reflectance levels close to 0.94, indicating no further improvement.

3.2.3 Impedance Mismatch Based Optimization

Studies have been conducted to enhance the efficiency of multilayer structures using Impedance Mismatch Based Optimization. This method is implemented in the MATLAB environment using genetic algorithm. One of the parameters entered before starting the optimization is the maximum thickness of a single layer. The initial level of maximum thickness was set at 2500 nm. It was later reduced to 1500 nm to investigate whether similar reflectance properties could be achieved with less thickness, and thereby more efficiently. Thickness outputs of the optimization are given in table 8.

Table 8. Thickness of individual layers as outputs of optimization with respect to number of layers and upper bound for layer thickness

Number of Layers	**Thickness of Individual Layers**										**Upper Bound for Layer Thickness**
4	1228	1500	1352	1500	-	-	-	-	-	-	1500
6	1227	1500	1347	1500	1348	1500	-	-	-	-	
8	1228	1500	1345	1500	1341	1500	1346	1500	-	-	
10	1227	1500	1344	1500	1217	100	100	1500	1313	1500	
12	1287	1500	100	1500	1343	1500	1336	1500	1324	1500	
	1293	1500	-	-	-	-	-	-	-	-	
4	1094	1970	1110	1989	-	-	-	-	-	-	2500
6	1090	1942	1117	1929	1115	1963	-	-	-	-	
8	1089	1924	1128	1901	1127	1900	1125	1933	-	-	
10	1090	1946	1120	1915	1117	1910	1105	1940	2205	2004	
12	1094	1970	1119	1928	1114	1918	1101	1937	2247	1921	
	1077	1910	-	-	-	-	-	-	-	-	

Reflectance spectrum of DBRs with varying thicknesses designed by Impedance Mismatch Based Optimization are given in figure 23. Average reflectance values are

given in table 9. Upper bound for layer thickness was set to 2500 nm through optimization runs.

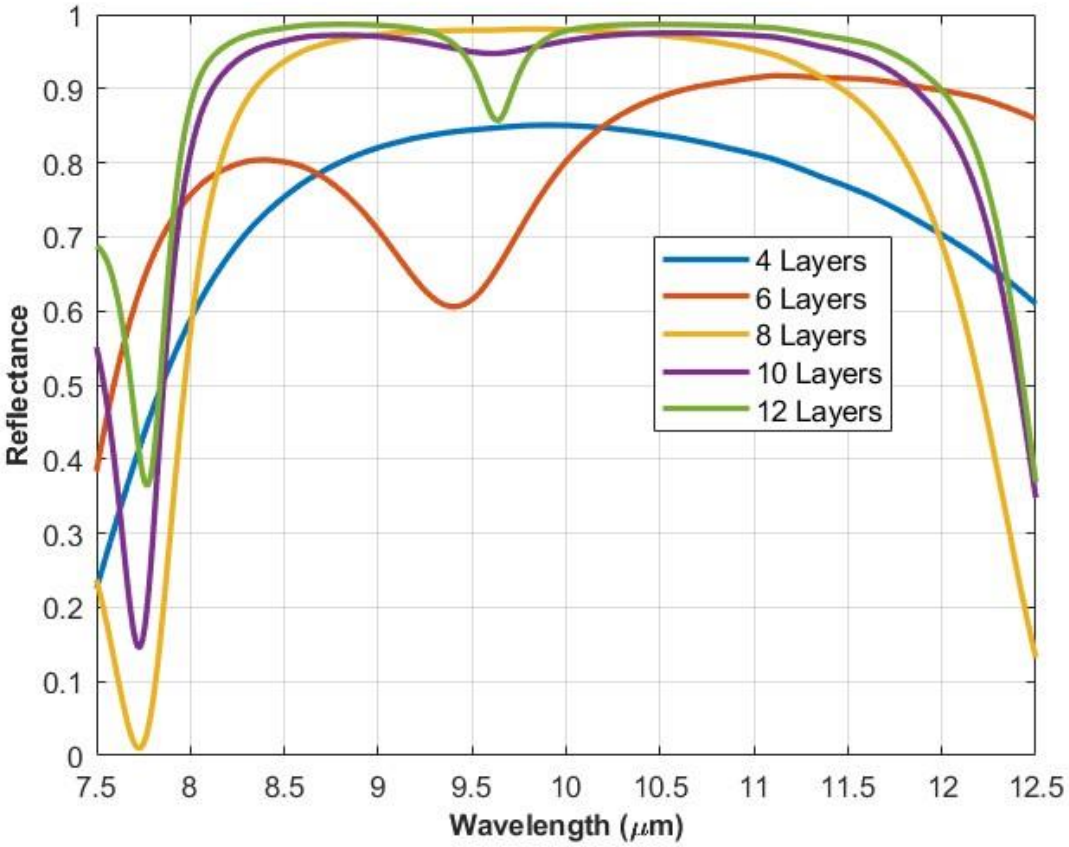

Figure 23. Reflectance spectrum of 4, 6, 8, 10, 12-layered coatings obtained by Impedance Mismatch Based Optimization with 2500 nm of upper limit for layer thickness

Table 9. Average reflectance and total thickness with respect to number of layers

Sample	Average Reflectance	Total Thickness of Layers (nm)
4-Layered Structure	0.79	6164
6-Layered Structure	0.89	9158
8-Layered Structure	0.93	12128
10-Layered Structure	0.95	16353
12-Layered Structure	0.96	19338

The results demonstrate that Impedance Mismatch Based Optimization can achieve very high reflectivity levels, even with a minimal number of layers. A structure comprising six layers yielded a reflectance of nearly 0.90. This level of reflectance required eight layers when utilizing the Tandem Approach and twelve layers with the Quarter-Wavelength Approach. Notably, the reflectance value of 0.97, achieved with twelve layers through optimization, surpassed the outcomes attainable by the other approaches within this study.

In the optimization study conducted to enhance the efficiency of the structures, the layer thickness was capped at 1500 nm. Utilizing Impedance Mismatch Based Optimization, the objective was to reduce the overall thickness while achieving reflectance values competitive with those of other approaches, thereby developing highly efficient structures. The spectral reflectance, average reflectance, and total thicknesses of the structures are presented in figure 24 and table 10, respectively.

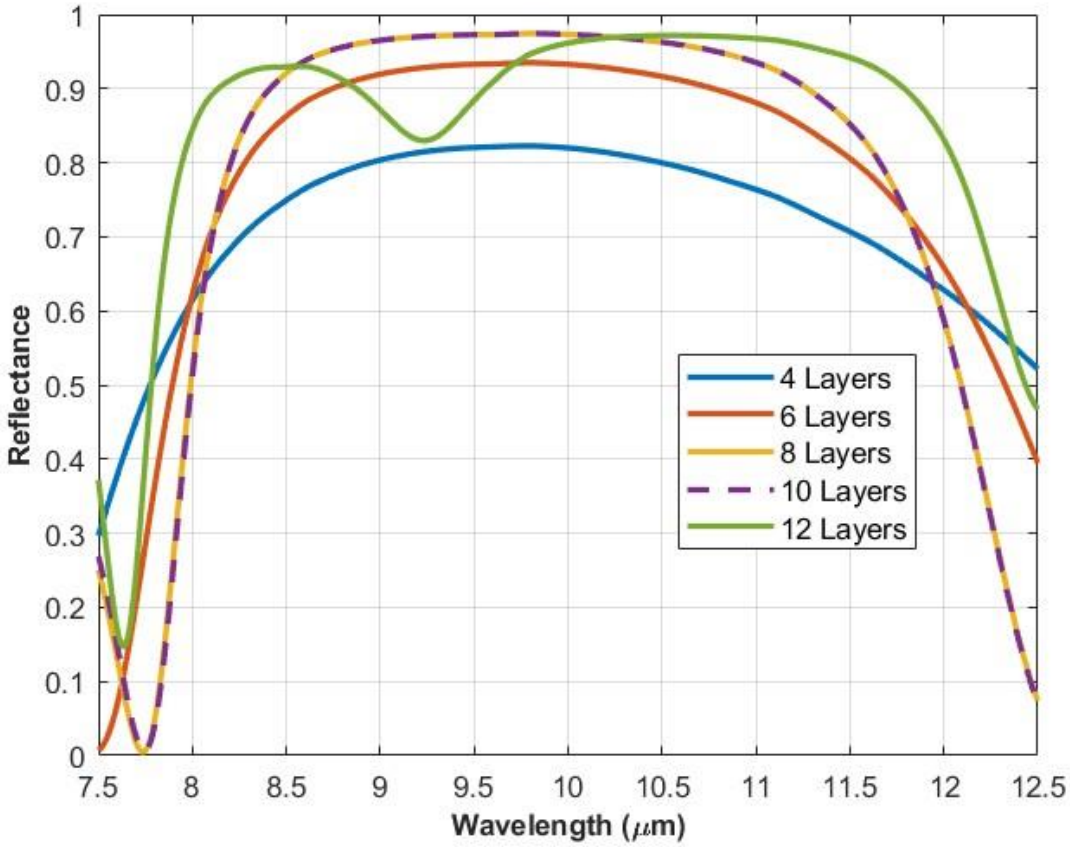

Figure 24. Reflectance spectrum of 4, 6, 8, 10, 12-layered coatings ontained by Impedance Mismatch Based Optimization with 1500 nm of upper limit for layer thickness

Table 10. Average reflectance and total thickness with respect to number of layers

Sample	**Average Reflectance**	**Total Thickness of Layers (nm)**
4-Layered Structure	0.76	5580
6-Layered Structure	0.87	8423
8-Layered Structure	0.91	11260
10-Layered Structure	0.90	11301
12-Layered Structure	0.92	15683

As seen in the results, optimization process yields structures with both high reflective properties and reduced total thickness compared to the quarter-wavelength approach. In comparisons of 8-layer structures, similar reflectance values to those achieved with the Tandem Approach were obtained, with a 13% reduction in thickness. However, the reflective characteristics provided by the Tandem approach with 10 and 12 layers were not replicated in this part of the study.

3.2.4 Spectrally Selective Wide-Band Reflectance

The studies progressed to a brief examination of the broadband reflectance properties of the structures. ZnS and MgF_2 have optical properties suitable for use in DBR structures in the MWIR band, making them preferred in broadband studies. The figure demonstrates the broadband reflection properties of the structure designed for the Long-Wave Infrared (LWIR) band using Quarter-Wavelength Approach and 12 layers. Average reflectance in the 3-5 μm, 5-8 μm and 8-12 μm are 0.32, 0.14 and 0.89 respectively. As expected, the performance of the structure designed for LWIR using the traditional method was quite inadequate in MWIR.

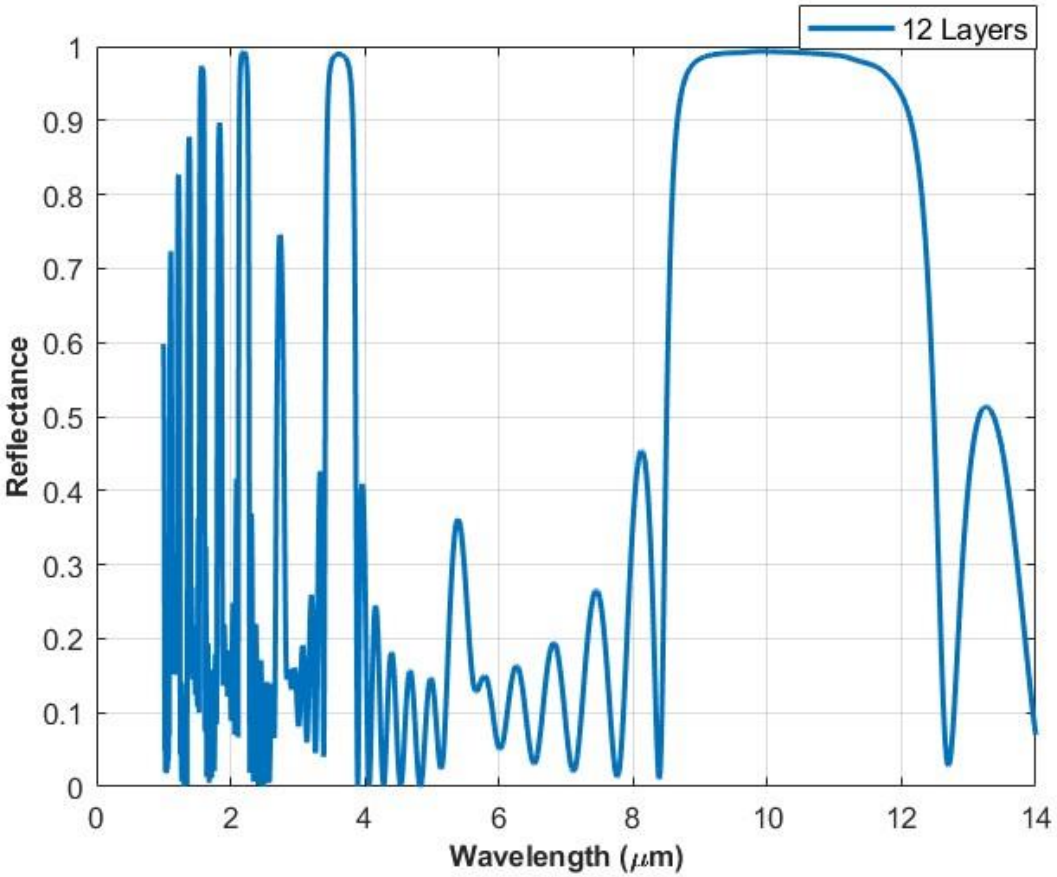

Figure 25. Broadband reflectance spectrum of LWIR design

Impedance Mismatch-Based Optimization was utilized to enhance performance and achieve a spectrally selective reflectance. The optimization parameters were fine-tuned to optimize high reflectance properties in the 3-5 and 8-12 bands. The outcomes are presented in the figure.

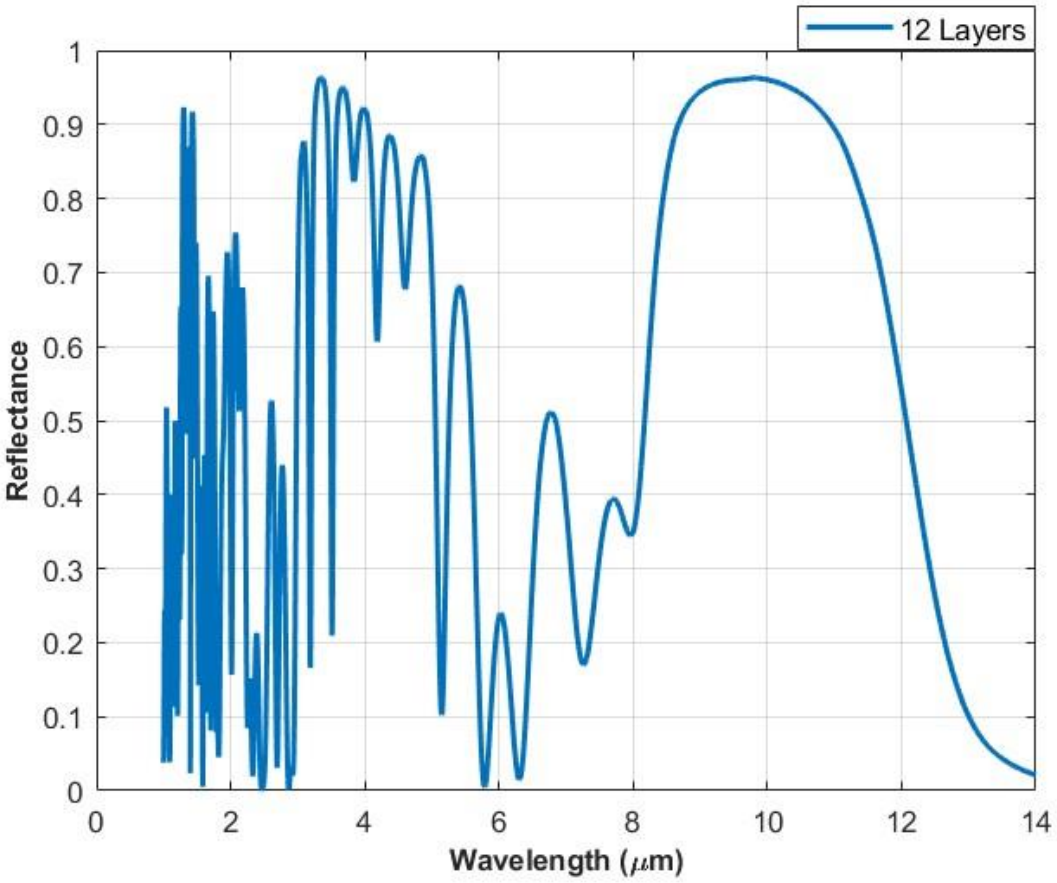

Figure 26. Broadband reflectance spectrum optimized structure

As seen in figure 26, optimization study significantly enhanced reflectivity in the targeted bands. The average reflectance achieved is 0.82 in the Mid-Wave Infrared (MWIR) band and 0.85 in the Long-Wave Infrared (LWIR) band. In the 5-8 μm band, which was not a focus of the optimization study, the reflectance level is maintained at 0.32. Through optimization, LWIR reflectance properties are largely maintained, whereas MWIR reflectance properties are enhanced nearly threefold.

3.3 Conclusion

Table 11. Results of Quarter-Wavelength Approach, Tandem Approach and Impedance Mismatch Based Optimization

	Quarter-Wavelength Approach*		**Tandem Approach****		**Impedance Mismatch Based Optimization – 1500 nm of Upper bound for Layer Thickness*****		**Impedance Mismatch Based Optimization – 2500 nm of Upper bound for Layer Thickness******	
Number of Layers	**Average Reflectance**	**Thickness of Stack (nm)**	**Average Reflectance**	**Thickness of Stack (nm)**	**Average Reflectance**	**Thickness of Stack (nm)**	**Average Reflectance**	**Thickness of Stack (nm)**
2	0.55	3256	-	-	-	-	-	-
4	0.78	6512	0.76	6547	0.76	5580	0.79	6164
6	0.85	9768	-	-	0.87	8423	0.89	9158
8	0.87	13024	0.89	13094	0.91	11260	0.93	12128
10	0.88	16280	-	-	0.91	11301	0.95	16353
12	0.89	19536	0.94	19641	0.92	15683	0.96	19338

The results from the studies in the Long-Wave Infrared (LWIR) section are presented in Table 11. Across all design approaches, it is evident that an increase in the number of layers, up to 12, correlates with enhanced reflective properties. Structures with 16 and 20 layers were also developed using the Tandem approach, showing a tendency for reflectance values to stabilize. Both optimization studies and the Tandem approach yielded higher reflectivity for an equivalent number of layers compared to the Quarter Wavelength approach. When comparing 8-layer structures, it is apparent that Impedance Mismatch Based Optimization not only provides high reflectivity but also reduces the thickness of the layers. In the optimization study, with the layer thickness limit set at 2500 microns, it was observed that increasing the number of layers could result in significantly high reflectivity levels. Examination of the 12-layer structures reveals that the layer thicknesses of the three different approaches are similar; however, optimization achieves higher reflectivity than the other structures. Furthermore, in the optimization study, limiting the maximum layer thickness to 1500 nm resulted in a substantial reduction in layer thickness while still achieving a reflectance above 0.90. Finally, it has been demonstrated that the optimization method can serve as an effective design approach for multiband applications, achieving reflectivity above 0.8 in two distinct spectral bands using only 12 layers.

4. TUNABLE REFLECTANCE

4.1 Problem Definition

VO_2 is a phase-change material that undergoes a transition from a dielectric phase to a metallic phase at approximately 67°C (Liu et al., 2024). This phase transition significantly alters its optical properties. The refractive index and extinction coefficient of VO_2 in its low-temperature dielectric phase and high-temperature metallic phase are presented in figures 27 and 28, respectively (Beanini et al., 2020).

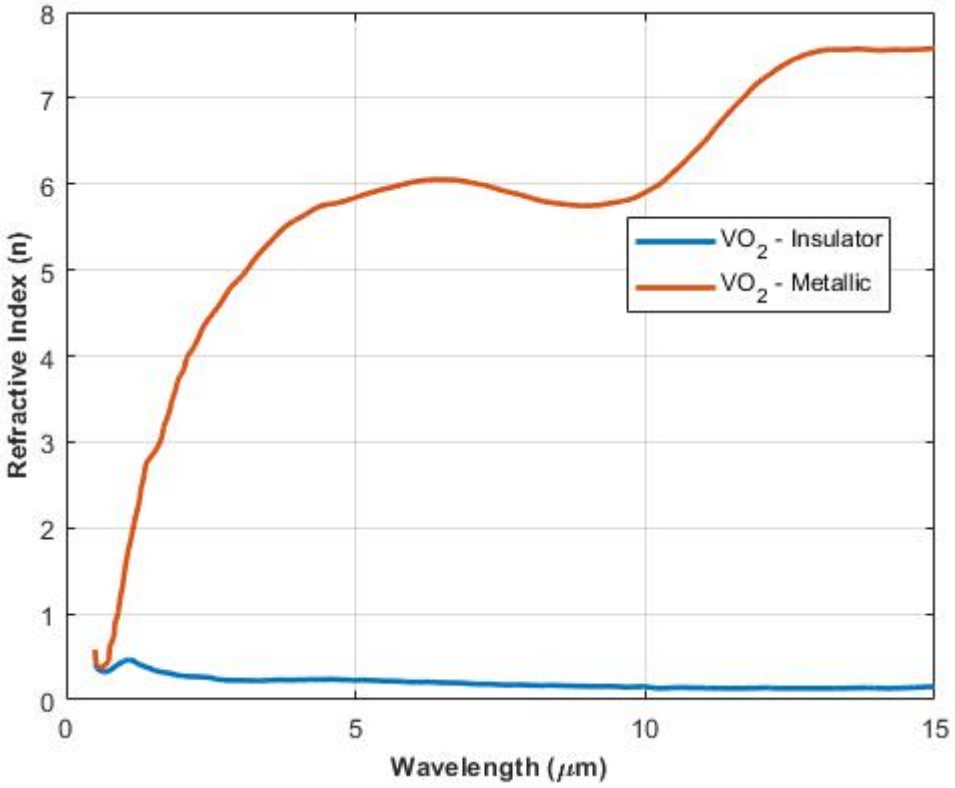

Figure 27. Refractive index of VO_2 in metallic and insulator phases

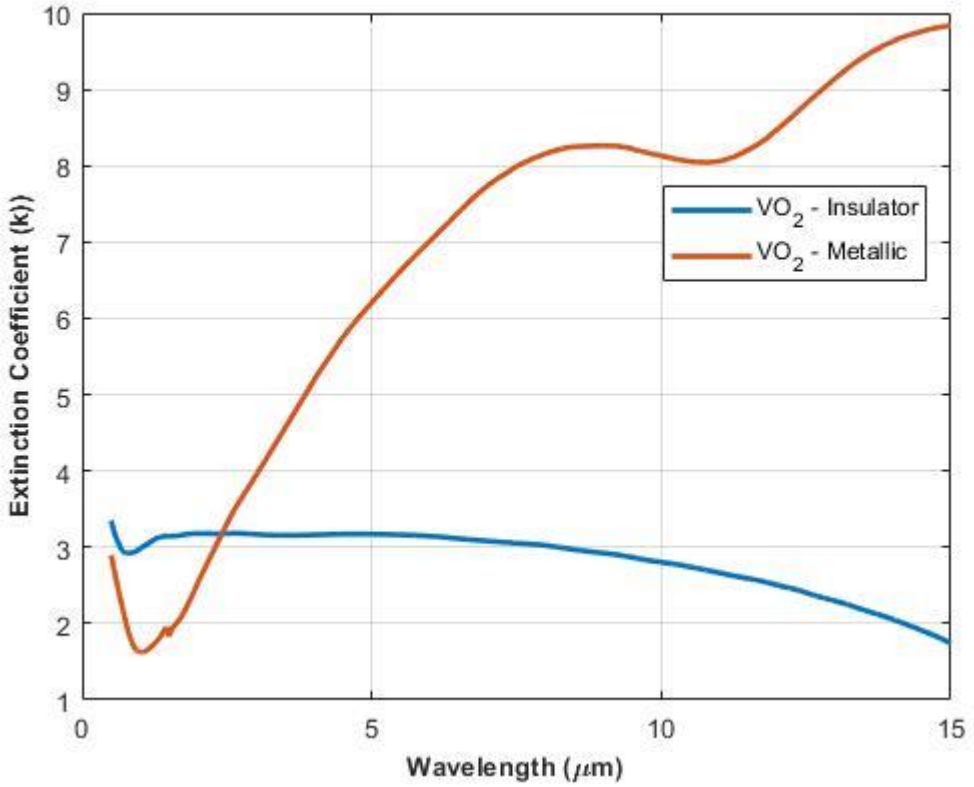

Figure 28. Extinction coefficients of VO_2 in metallic and insulator phases

Phase-change properties have the potential to enable switching capabilities in optical applications. In recent years, there has been a growing number of studies exploring the use of these properties in various optical systems. Switchable spectral response properties have attracted significant attention for thermal management in space applications. Kong et al. (2024) investigated the spectral behavior of a structure incorporating VO_2 within thin-film designs across broad wavelength bands. Their study demonstrated adjustable reflectance in the NIR, MWIR, and LWIR regions. The results revealed that the phase transition between the metallic and insulating states of VO_2 in thin-film form is particularly effective at higher wavelengths. Reflectance exhibits significant variation in the MWIR and LWIR regions, with notable changes also observed in the NIR. Beanini et al. (2020) calculated the high-temperature and low-temperature optical properties of VO_2 and utilized these properties in their designs for space applications. The combination of VO_2 with Au, CaF_2, and Si_3N_4 achieved an approximate 65% change in emissivity across

the 2.5–25 μm wavelength range. Both studies demonstrated excellent results in achieving reflectance adjustment, particularly at higher wavelengths.

This section focuses on the utilization of the phase-change properties of VO_2 within a narrower wavelength range in the NIR band. The reflectivity difference between the two states of an ideal system operating in the NIR and providing an adjustable optical response is depicted in figure 29.

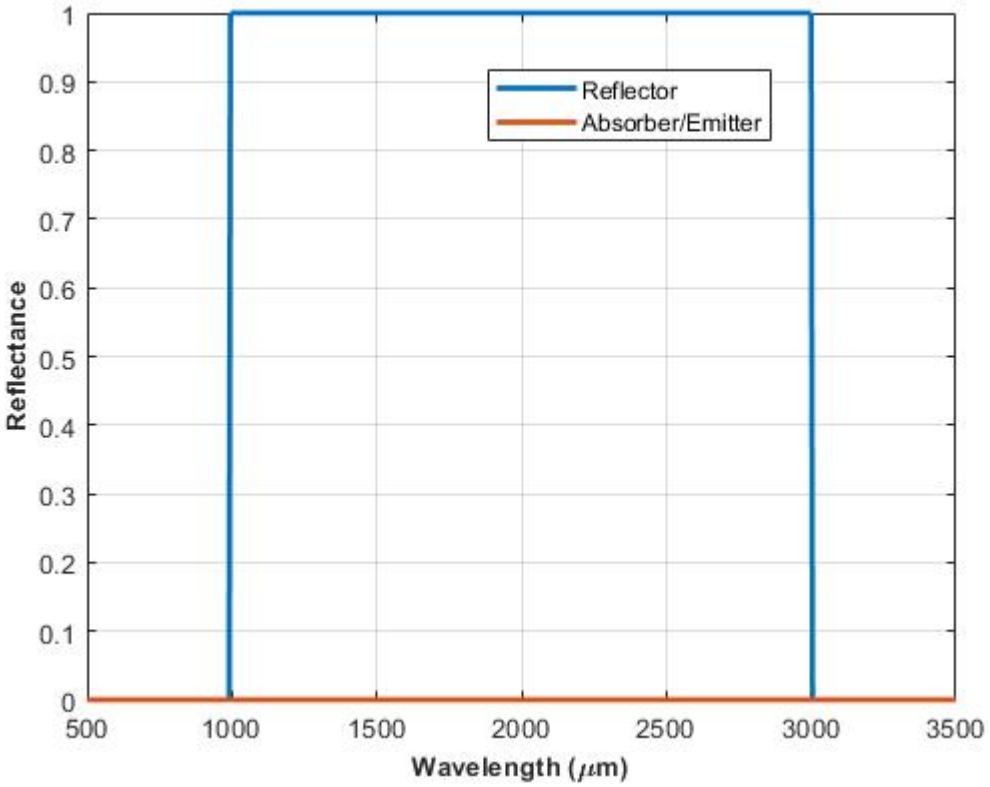

Figure 29. Reflectivity difference between two states

Conical nanostructures are widely used design schemes to achieve high absorption and emission in the visible and NIR regions. By optimizing the geometries and periodicities of tungsten (Guo et al., 2021) and titanium nitride (Huo et al., 2018; Wang et al., 2017), nanocones with metallic properties, minimum reflectivity in the visible and NIR regions can be achieved. Habil et al. (2022) demonstrated 99% absorption up to 4 μm using more complex nanoconical structures. These studies indicate that efficient absorptive systems can be developed in the visible and NIR wavelength ranges using conical structures with metallic properties.

In this section, VO_2 cones are incorporated onto traditional Bragg reflectors, as shown in figure 30. High reflectivity is achieved at 2 μm, the midpoint of the NIR region, using Bragg reflectors. The goal is for the VO_2 cones to transform the structure into an absorber/emitter when transitioning to the high-temperature metallic phase.

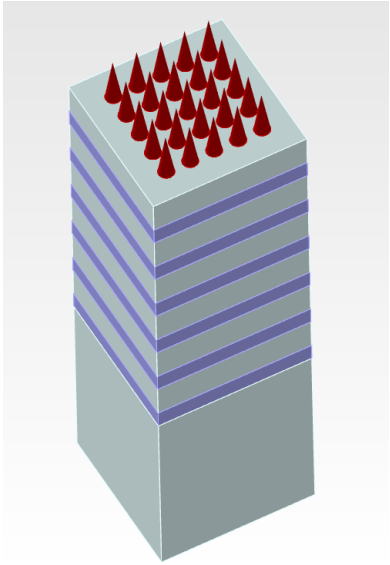

Figure 30. VO_2 cones on DBR

Effect of geometry and periodicity of VO_2 cones on the spectral response is investigated. The reflectivity of the DBR+VO_2 system is aimed to be minimized when VO_2 is in its high temperature metallic phase.

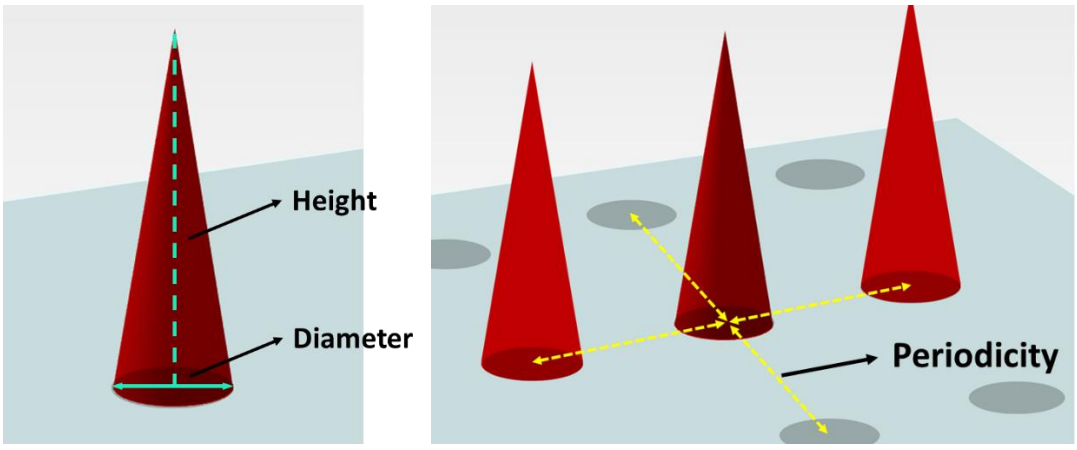

Figure 31. Parameters of VO_2 cones

4.2 Results

VO_2 cones are placed on DBRs designed for the 2 μm wavelength, which is the midpoint of NIR. TiO_2 and SiO_2 are utilized as high index and low index material respectively. The reflectance spectrum of the neat state of the DBR structures used under VO_2 is given in figure 32. The structures consisting of TiO_2 and SiO_2 films as high index and low index materials, respectively, are reflective at a level close to the maximum at the design wavelength, as might be expected.

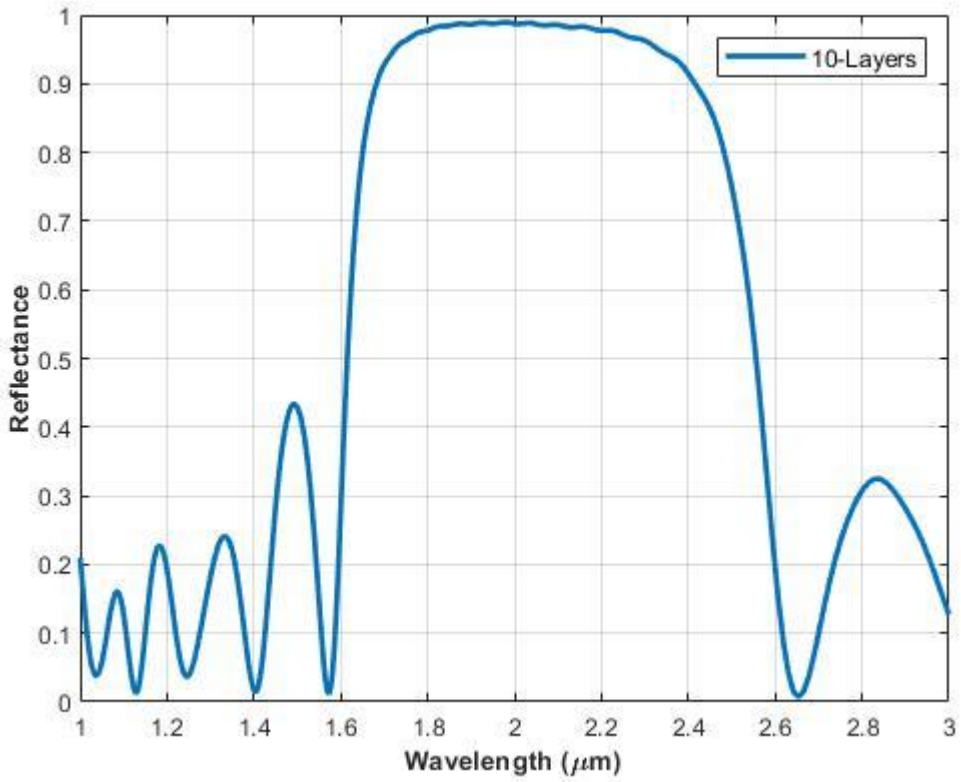

Figure 32. Reflectance spectrum of DBR in NIR

VO_2 cones of different heights, widths and periodicities are used on the DBR. It is aimed to minimize the reflectivity at this wavelength with the absorber properties that VO_2 will provide when it is in the metallic phase. How different cone diameters affect the reflectivity of the DBR + VO_2 structure when the VO_2 cones are in the insulating and metallic phases are given in figure 33 and 34, respectively.

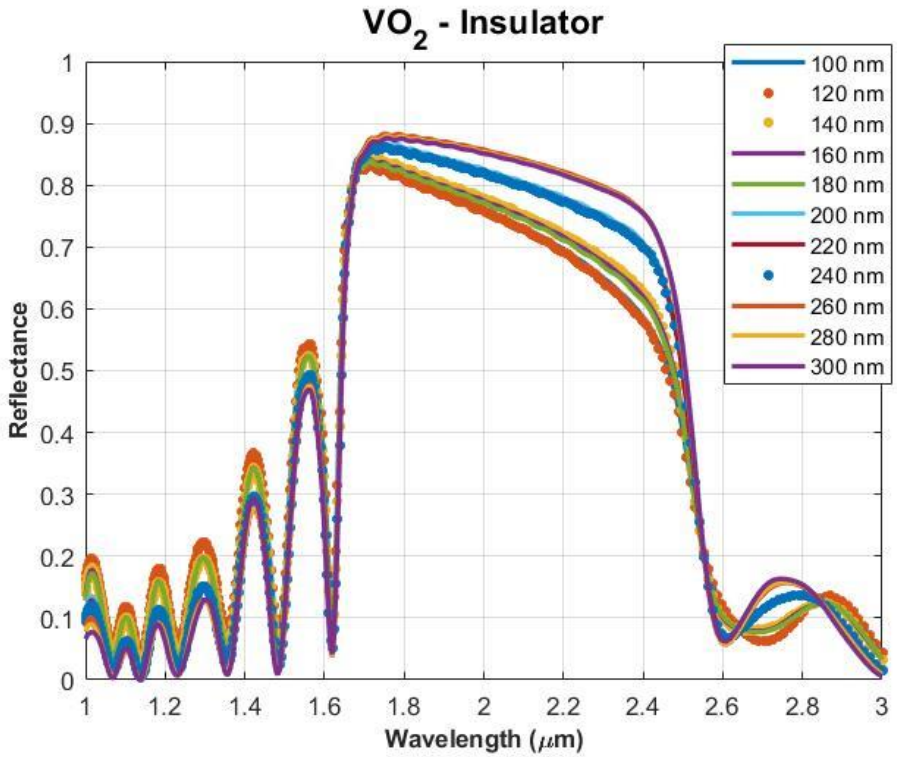

Figure 33. Reflectance spectrum of DBR+VO_2 with varying cone diameter

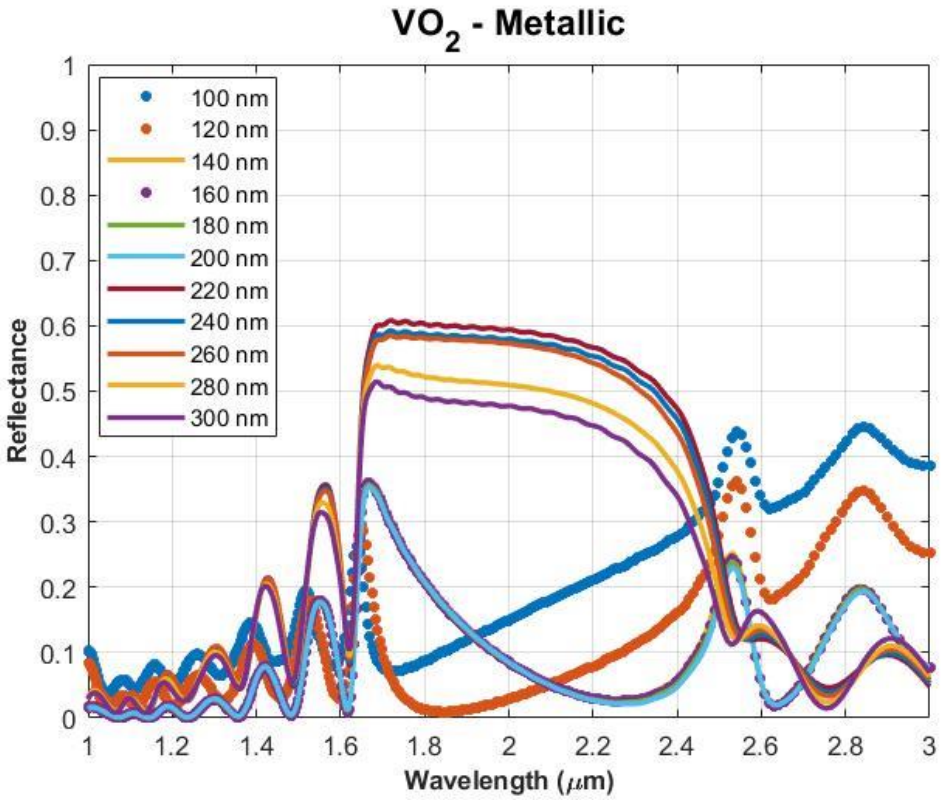

Figure 34. Reflectance spectrum of DBR+VO_2 with varying cone diameter

Results reveals that when VO_2 is in its insulating phase, and the DBR + VO_2 structure is in the high-reflectivity state, it provides slightly lower reflectivity compared to pure DBR. However, when VO_2 transitions to its metallic phase, a significant reduction in reflectivity is observed. Among the absorber structures evaluated, the performance is notably better when the radius is 200 nm or smaller. In particular, radius values ranging from 120 to 200 nm are suitable for achieving effective absorptive structures.

After the cone radius, the effect of cone heigh is investigated. The spectral behaviors of DBR + VO_2 – Insulator and DBR + VO_2 – Metallic structures are given in figure 35 and 36, respectively.

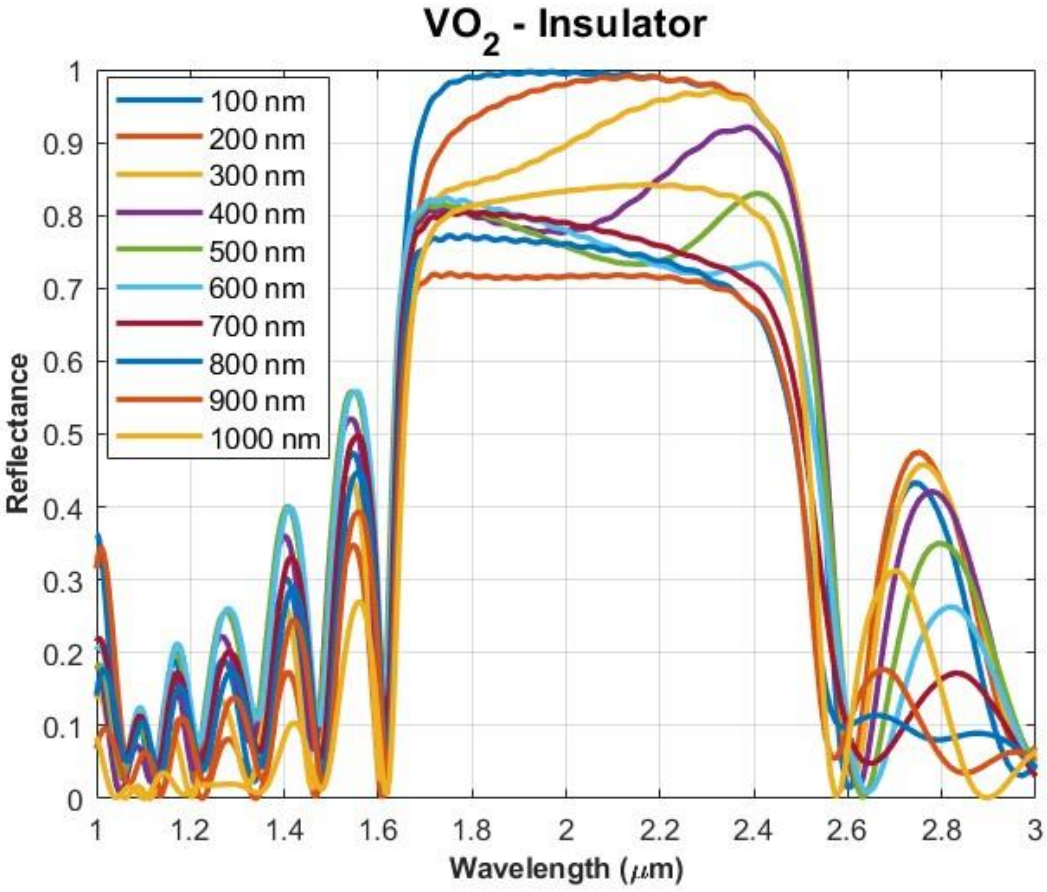

Figure 35. Reflectance spectrum of DBR+VO_2 with varying cone height

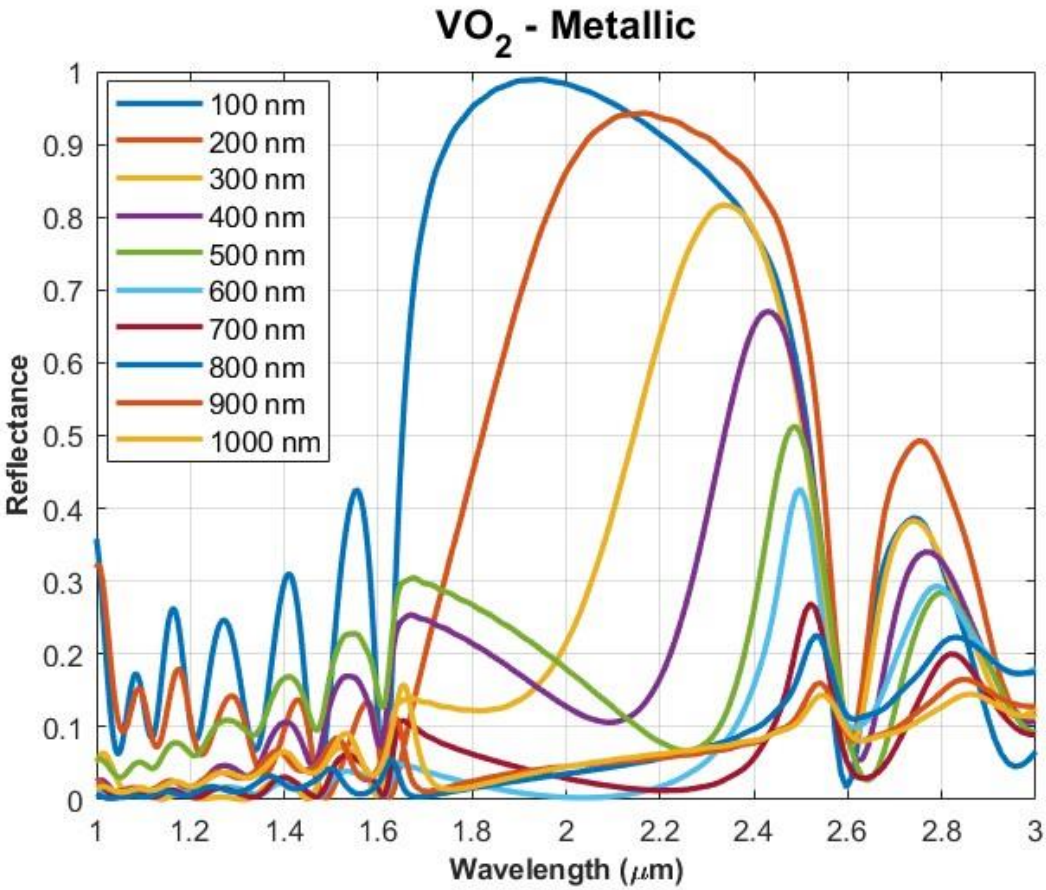

Figure 36. Reflectance spectrum of DBR+VO_2 with varying cone height

The results indicate that the DBR + VO_2 - Insulator structure exhibits reflectivity values ranging from 0.7 to approximately 1 within the 100–1000 nm cone height range. These results are acceptable for reflective mode. Conversely, for the DBR + VO_2 - Metallic structure to achieve low reflectivity, the cone height must exceed 600 nm.

Finally, the spectral behavior of VO_2 was investigated for low and high temperature phases by changing the periodicity of the cones between 7.5 nm and 22.5 nm. The reflectivity of DBR + VO_2 – Insulator and DBR + VO_2 – Metallic structures are given in figure 37 and 38, respectively.

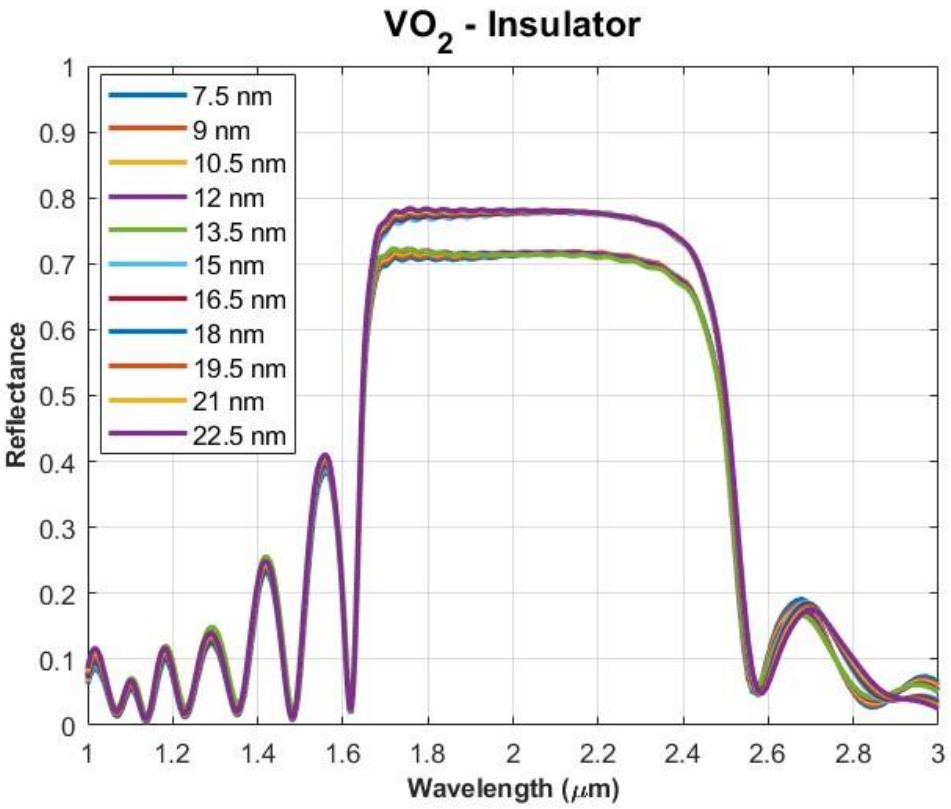

Figure 37. Reflectance spectrum of DBR+VO_2 with varying periodicity

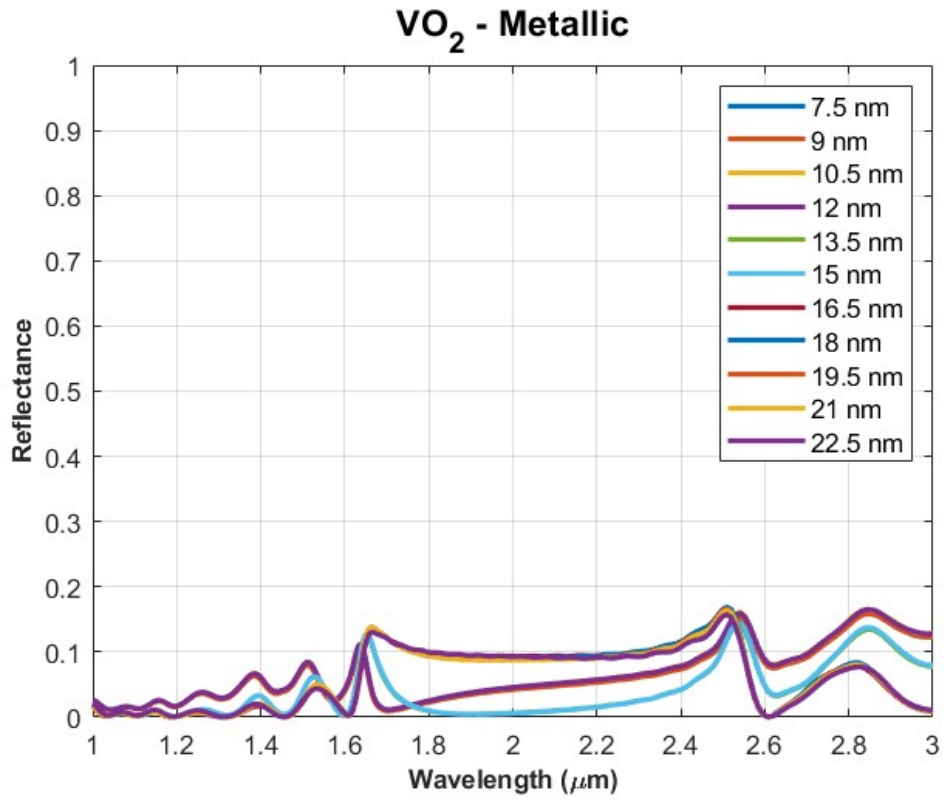

Figure 38. Reflectance spectrum of DBR+VO_2 with varying periodicity

Similar to the height scan results, the change in periodicity had little effect on reflectivity when VO_2 is in its low-temperature insulating phase. Likewise, when VO_2 was in the metallic phase, the spectral behavior of the structure was minimally influenced by changes in periodicity. The lowest reflectivity level was achieved at a periodicity of 15 nm.

The comparison of the reflectivity properties of the structure obtained as a result of parametric scanning at high and low temperatures can be seen in Figure 39.

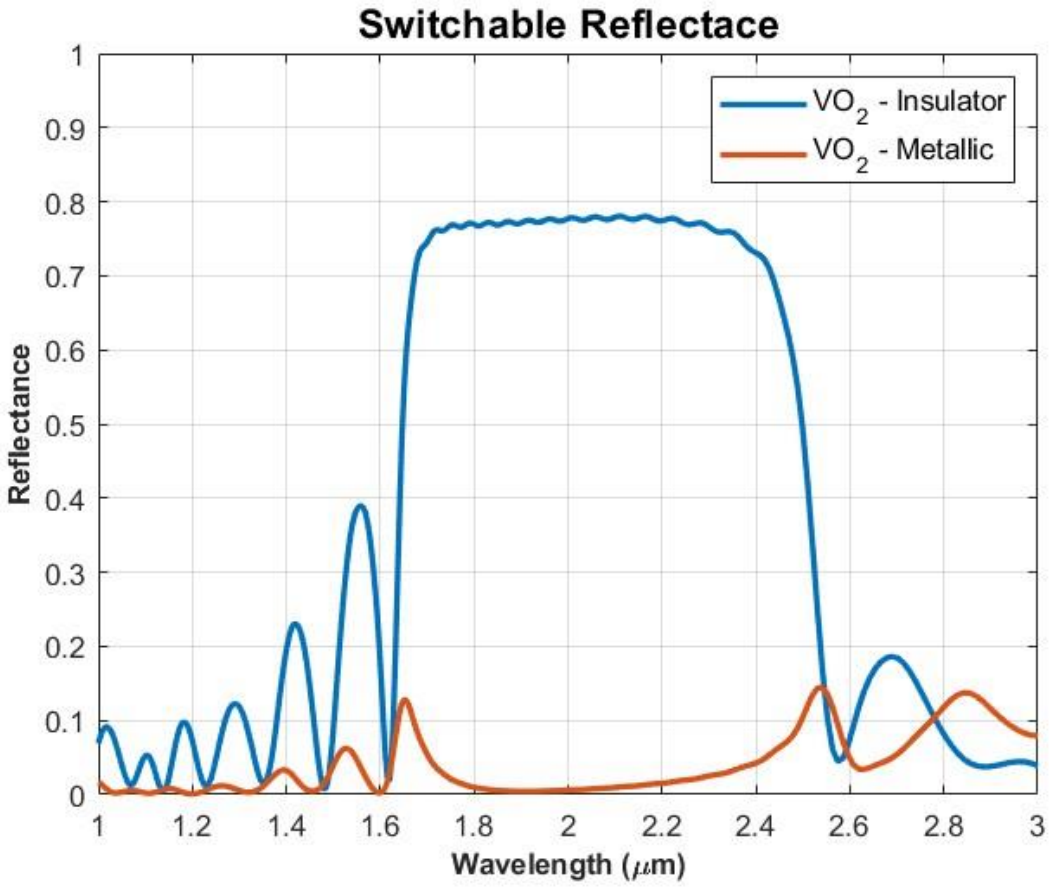

Figure 39. Reflectance spectrum of the structure when VO_2 is in different phases

When the cone diameter is 160 nm, the height is 900 nm and the periodicity is 15 nm, the reflectivity of the DBR + VO_2 structure is close to 0.8 around 2 µm when VO_2 is in the low temperature insulating phase. When VO_2 is in the high temperature metallic phase, the reflectivity values of the structure almost drop to 0.

The transmittance spectra of VO_2 in its low-temperature and high-temperature phases are presented in Figure 41. As observed, in both phases, there is no transmittance within the

wavelength range where the multilayer film structure exhibits reflectivity. In the absorber/emitter mode, transmittance is also reduced at other wavelengths.

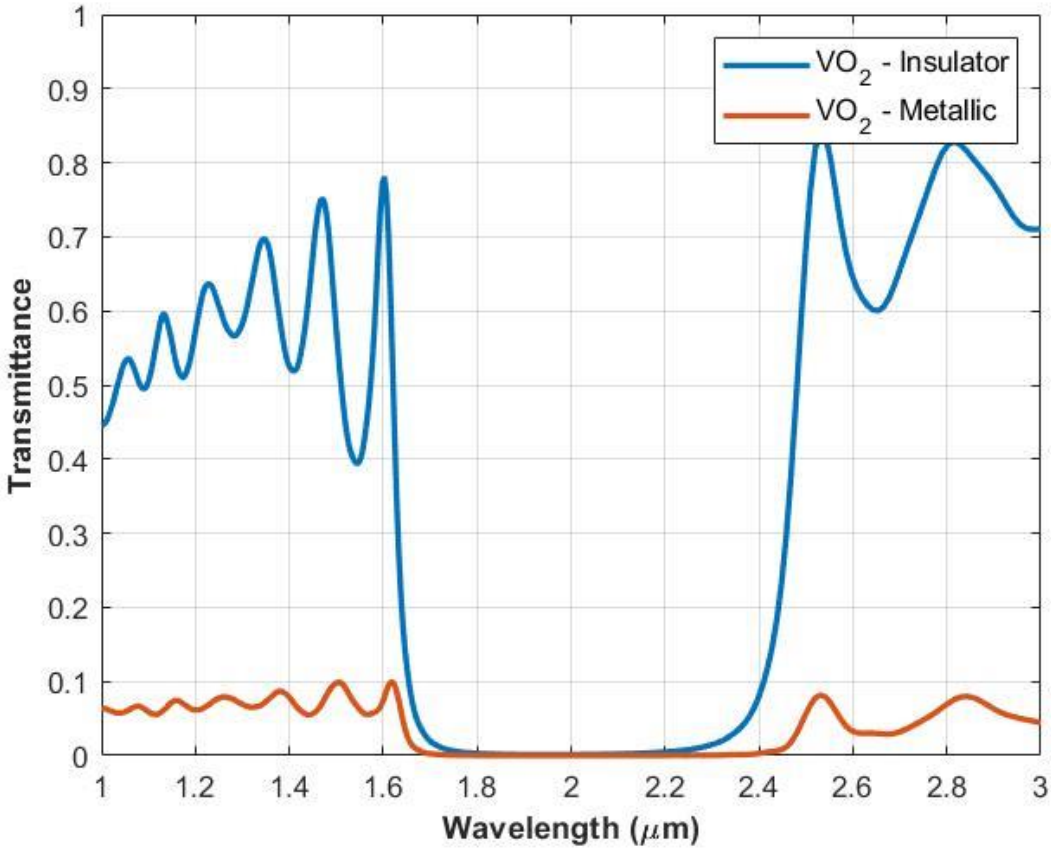

Figure 40. Transmittance spectrum of DBR+VO2 in absorber/emitter mode

For comparison, a VO_2 film with the same thickness as the cone height in the switchable reflectance case was placed on the multilayer stack, and its reflectance spectrum was analyzed. The results showed that the absorber/emitter properties exhibited by VO_2 in its metallic phase—within this wavelength range and thickness—cannot be replicated using the film form alone.

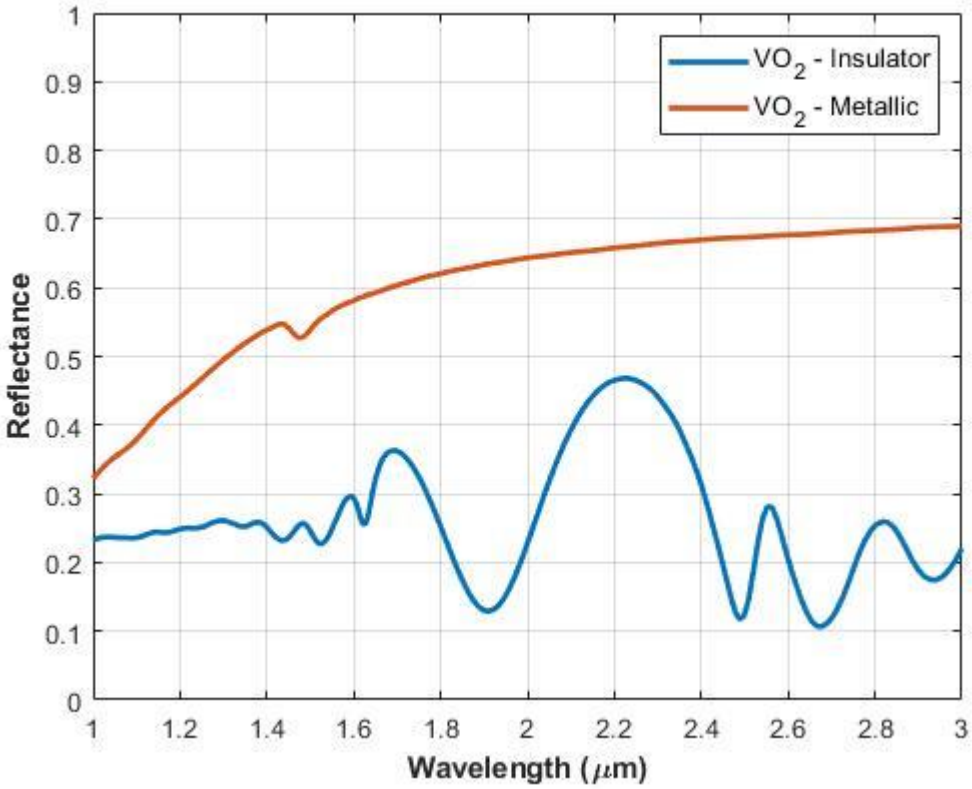

Figure 41. Reflectance spectrum of DBR + VO2 film when VO2 is in different phases

Finally, to investigate the underlying mechanism of the absorber/emitter behavior in the metallic phase, the electric field distributions on the conical structure were analyzed at different wavelengths. The results indicate that distinct regions of the cone exhibit resonance at different wavelengths.

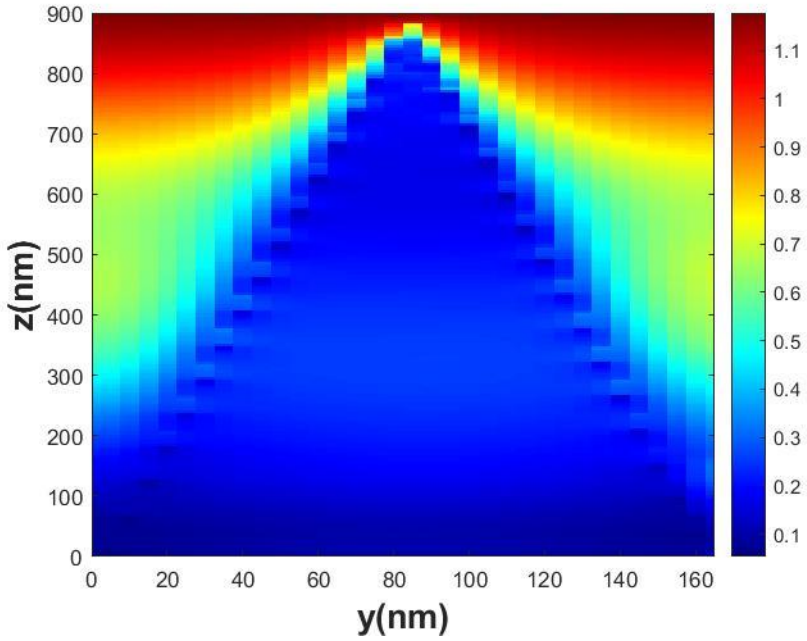

Figure 42. E-field Distribution at 1500 µm

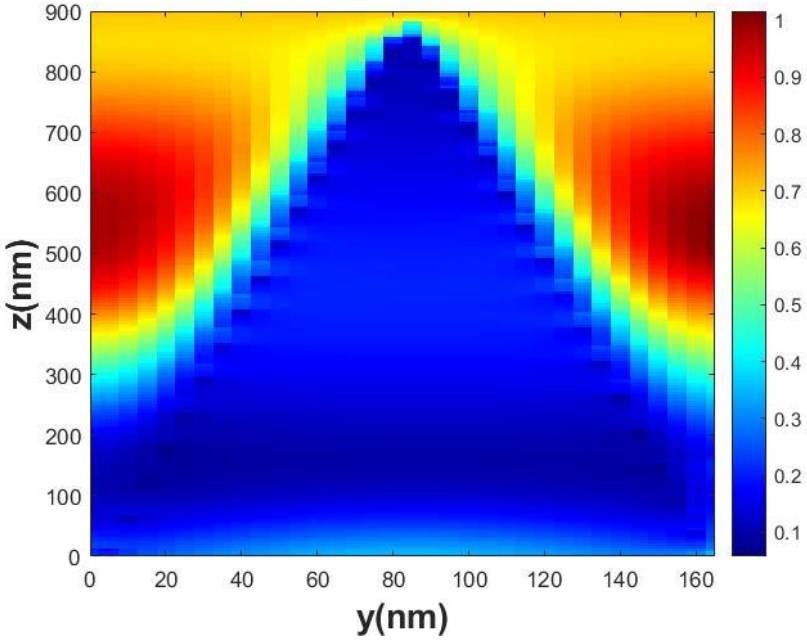

Figure 43. E-field Distribution at 1750 µm

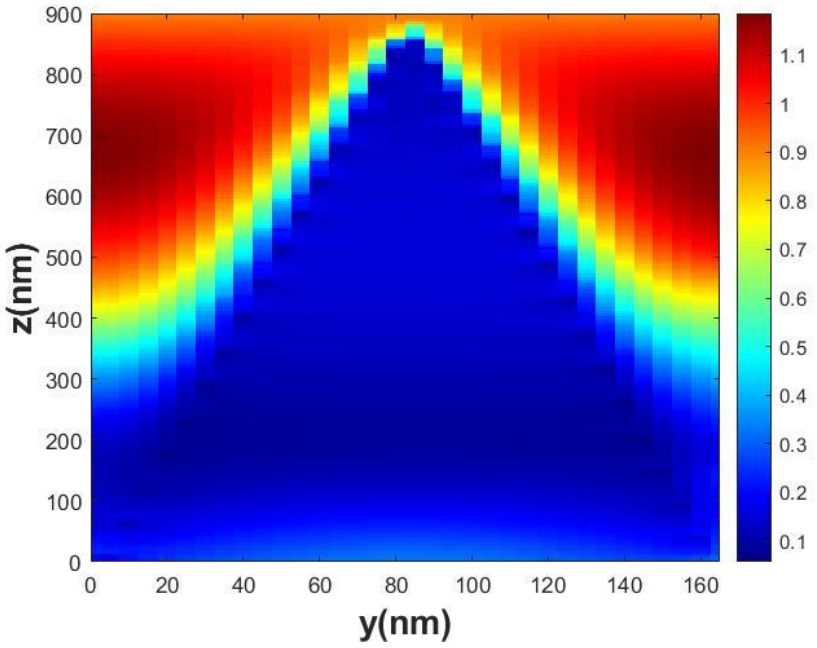

Figure 44. E-field Distribution at 2000 µm

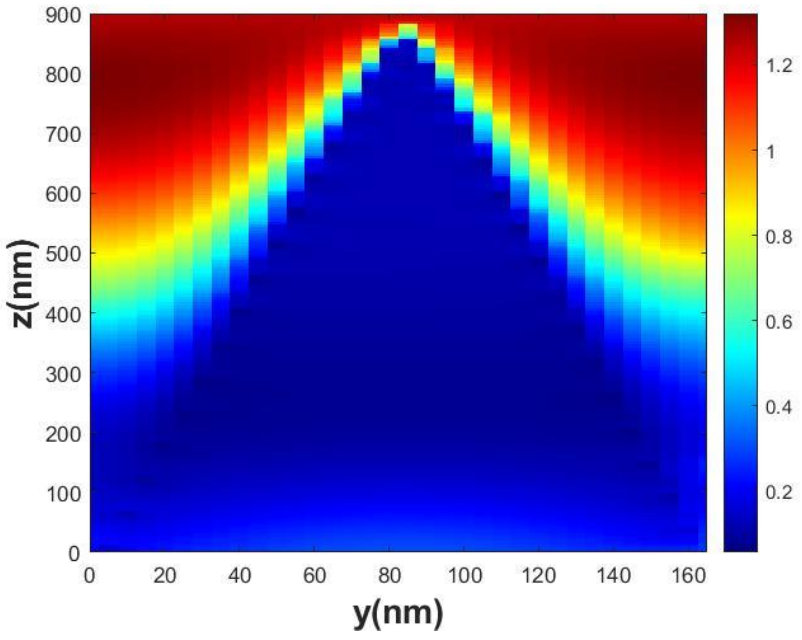

Figure 45. E-field Distribution at 2250 µm

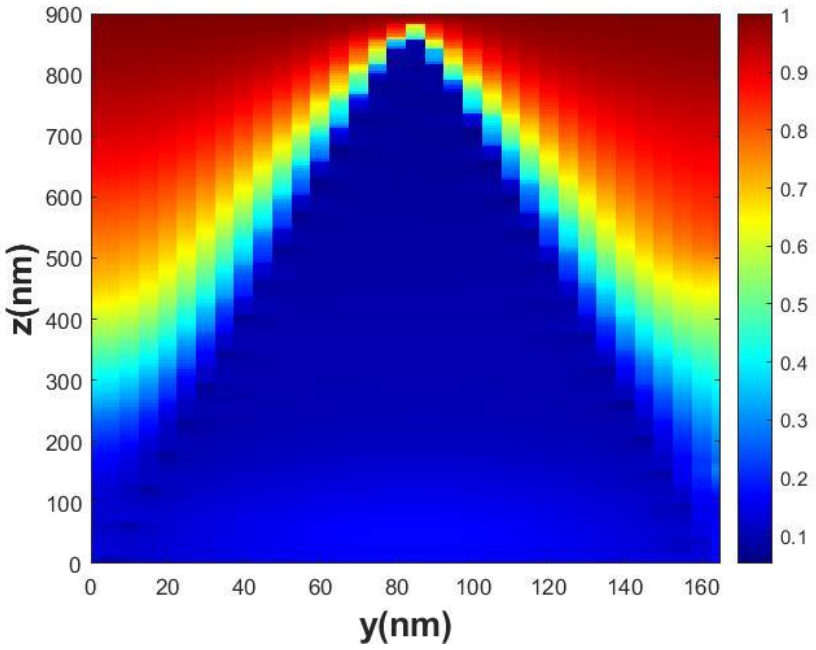

Figure 46. E-field Distribution at 2500 µm

4.3 Conclusion

It is observed that the optical properties of VO_2, which change with the temperature-dependent phase transformation, can cause very large differences in spectral behavior when added to optical designs in conical form. When the temperature of conical VO_2 increased to 67 degrees, the reflectivity, which was 0.8, decreased to almost 0. Metallic phase VO_2 showed absorptive properties similar to the studies in the literature. Conical VO_2 can be used to obtain switchable reflectivity in the NIR band and to provide a temperature-triggered transition between reflective and absorptive structures.

5. CONCLUSION & FUTURE WORK

5.1 Conclusion

In this thesis, spectral reflectivity and emissivity of multilayer thin films are investigated using modelling and design. Both TMM and FDTD are utilized. Through this combined analytical and numerical investigation, effectiveness of the proposed techniques are examined and confirmed.

The effects of different design approaches on the reflectivity performance of thin films are investigated. First, single-band studies are conducted. Then, the usability of design approaches that increase efficiency in multi-band applications is questioned. Finally, innovative approaches are used to provide functionality to thin-film structures.

Initially, relatively easy single band studies are started and focused on MWIR. Thin films are designed using traditional quarter wavelength approach, tandem approach and impedance mismatch based optimization and their spectral behaviors are compared. It is seen that the performance of traditional design method could be improved with both tandem approach and optimization method. While tandem approach provided very high reflectivity as the number of layers increased, it was seen that optimization method performed better than both design approaches with the same number of layers, i.e. increased efficiency.

Secondly, MWIR studies are extended to LWIR. Materials with proper optical properties are investigated for DBRs to operate in the 8-12 μm band. It is seen that the refractive indexes and extinction coefficients of ZnS and MgF_2 are suitable for use in LWIR and even MWIR. It is observed that the traditional design method provided better performance in LWIR, so although the Tandem approach and optimization method provided improvements, the performance and efficiency increase are not at the level of MWIR. The

consistency of the modeling methods and the performances provided by the design methods are demonstrated in two separate sections with single band studies.

The efficiency improvements achieved through the optimization method, along with its applicability across different wavelength bands, support the feasibility of developing efficient structures for wide-band applications. ZnS and MgF_2 are chosen for multi-band studies due to their optical properties, which are well-suited for operation in the MWIR and LWIR bands. For comparison purposes, the wide-band performance of the structure developed in the LWIR band is evaluated. The thin-film structure, optimized for thickness using the proposed method, demonstrated high reflectivity levels in the MWIR and LWIR bands while suppressing reflectivity in the 5–8 μm wavelength range, which lies outside the target band. The study confirms that Impedance Mismatch-Based Optimization is a versatile and effective design method for multi-band applications.

Finally, switchable reflectivity in the NIR band is achieved by combining DBRs with periodic conical VO_2. Since the primary focus of studies in this band was on reflectance changes between the high- and low-reflectance phases, the impact of design methods on thin-film performance is not extensively investigated. VO_2, known for its phase-change properties, is integrated into thin films as periodic conical structures. When VO_2 was in the high-temperature metallic phase, its conical geometry enabled it to function as an absorber, significantly suppressing the reflectivity of the design. In contrast, during the low-temperature insulating phase of VO_2, the structure exhibited no notable effect on reflectivity performance.

In conclusion, the performance of thin-film stacks is enhanced for single-band operations, multiband structures is successfully designed, and switch functionality is integrated into thin films.

In single-band studies, results consistent with the existing literature and expected outcomes are obtained. Reflectivity performance improved as the number of layers increased. The tandem approach, commonly utilized in solar panels, enhanced reflectivity in the MWIR and LWIR bands. While Impedance Mismatch-Based Optimization is a previously established method (Heavens, 1986), it was applied to the MWIR and LWIR bands for the first time in this study, and its effectiveness is demonstrated. Additionally,

this method is employed for the first time in the development of spectrally selective multiband designs, proving its applicability in such contexts.

The phase-change properties of VO_2 have attracted attention for optical applications; however, these studies primarily utilized VO_2 in thin-film form (Liu et al., 2024; Beanini et al., 2020). Similarly, conical metallic structures have been investigated due to their absorber properties (Wang et al., 2017). In this study, the phase-change properties of VO_2 are combined with conical geometry, enabling it to function as an absorber in its metallic phase. While VO_2 is theoretically well-suited for the development of functional structures, no prior studies have been identified on its fabrication in a conical geometry. If manufacturing techniques to produce conical VO_2 structures can be developed, these properties could be translated into practical applications.

5.2 Future Work & Limitations

Within the scope of this study, it has been demonstrated that the proposed optimization method is suitable both for enhancing efficiency and for the development of multiband filters. Future research can be expanded by utilizing a broader material library and exploring thin-film structures composed of more than two materials. Studies on efficiency and selective filtering may also be extended toward broader spectral ranges, including hyperspectral applications.

Additionally, the literature shows that alternative fabrication approaches can lead to increased efficiency. For instance, as demonstrated by Leem et al. (2014), the optical properties of hollow TiO_2 structures can be incorporated into simulation tools to achieve higher performance with fewer layers.

The methods highlighted in both the literature and this simulation study need not be limited to reflective structures alone; they can also be adapted to obtain different optical responses. For example, as shown in the work of Xie et al. (2025), these methods can be applied to the development of emitter structures or to achieve more band-specific responses.

Various methods can be employed to fabricate Bragg reflectors. These include physical vapor deposition techniques such as e-beam evaporation and sputtering, as well as chemical vapor deposition, atomic layer deposition, and pulsed laser deposition.

Thin-film deposition methods enable highly controlled fabrication with low thickness tolerances. Among these, atomic layer deposition offers the highest level of control, allowing for layer thickness precision at the angstrom scale (George, 2010). Sputtering (Colin et al., 2020), electron-beam evaporation (Perego et al., 2006), and chemical vapor deposition (Obraztsov et al., 2007) methods also provide thickness control within a few nanometers. However, a key disadvantage of these methods is the extended production time as film thickness increases. This is particularly significant for LWIR applications, which require thicker films; producing such films using these methods can be time-consuming and lead to increased manufacturing costs.

Studies are being conducted on the sol-gel spin coating method as a means to reduce production time and cost. Although this method offers less control compared to conventional thin-film deposition techniques, studies involving thin films have demonstrated that thickness variation can be limited to just a few nanometers (Rabaste et al., 2002; Hinczewski et al., 2005). However, one of the main limitations of the sol-gel spin coating method is the relatively small surface area that can be uniformly coated.

In the analyses, VO_2 cones were modeled as ideal structures in the simulation tools; in other words, surface roughness was not included as an input parameter. However, literature reports indicate that surface roughness can significantly influence spectral responses in both the visible and infrared bands, and in some cases, this effect can be harnessed for beneficial outcomes. For example, Prouzfam et al. (2018) demonstrated that isotropic and anisotropic roughness profiles can be employed to develop spectrally selective absorbers. In their study, they enhanced the absorbance of a flat tungsten surface by incorporating surface roughness into the simulations for wavelengths below 1500 nm. In a similar manner, future calculations could incorporate surface roughness into the modeling of conical structures, particularly to investigate its effect on the spectral response in the absorber–emitter phase.

In this study, the optical parameters of VO_2 were adopted from the work of Beanini et al. (2020). The low-temperature properties were measured at 25 °C, while the high-

temperature properties were obtained at 100 °C. The phase transition temperature of VO_2 is approximately 67 °C; however, this temperature can be tuned through various doping techniques (Yang et al., 2022). Additionally, it has been reported in the literature that nanoscale effects can also influence the transition temperature. Nakano et al. (2012) measured the phase transition temperature of VO_2 as 67 °C for a 70 nm-thick film, whereas it was observed near room temperature for a strained film with a thickness of 10 nm. Whittaker et al. (2009) reported that the transition temperature could be further reduced using wire-type nanostructures.

It is also well known that the geometric parameters of nanostructured particles influence their optical properties (Kelly et al., 2003). These characteristics, widely utilized in plasmonic technologies, have been employed to tune the resonance frequency of nanoparticles (Jain et al., 2006). However, there are only a limited number of studies in the literature that directly investigate the effects of the geometric parameters of VO_2 cones on spectral response. Lu et al. (2024) used FDTD simulations to demonstrate that the height, upper-to-lower base ratio, and porosity of discrete nanocones affect transmittance spectra and thermochromic performance at wavelengths below 2.5 μm. They subsequently fabricated parabolic nanocone arrays using a two-step process: in the first step, the film was deposited, and in the second, it was transformed into a nanocone array. Although their experimental results did not establish a direct correlation between the height of the conical arrays and optical performance, they showed that the thickness of the film used to form the cones had an impact on optical behavior.

In this study, the base diameters of the conical VO_2 structures exceed 100 nm and decrease linearly toward the tip, approaching zero. When considered independently, the base regions exhibit geometric dimensions where nanoscale effects are negligible, whereas the tip regions are likely to exhibit pronounced nanoscale behavior. The phase transition significantly alters the optical properties of VO_2. Therefore, investigating whether the transition temperature and optical properties of conical VO_2 structures vary as a function of nanoscale geometric parameters would be valuable for gaining deeper insight into the material's behavior.

BIBLIOGRAPHY

Al-Azzawi, A. (2018). *Physical optics: principles and practices*. CRC Press.

Balabanian, N. (1955). Impedance matching (correspondence). *IRE Transactions on Microwave Theory and Techniques*, *3*(4), 53-54.

Beaini, R., Baloukas, B., Loquai, S., Klemberg-Sapieha, J. E., & Martinu, L. (2020). Thermochromic VO2-based smart radiator devices with ultralow refractive index cavities for increased performance. *Solar Energy Materials and Solar Cells*, *205*, 110260.

Bergthold, M., Wasserman, D., & Muhowski, A. J. (2022). Plasmon-enhanced distributed Bragg reflectors. *Infrared Physics & Technology*, *125*, 104236.

Colin, J., Jamnig, A., Furgeaud, C., Michel, A., Pliatsikas, N., Sarakinos, K., & Abadias, G. (2020). In situ and real-time nanoscale monitoring of ultra-thin metal film growth using optical and electrical diagnostic tools. *Nanomaterials*, *10*(11), 2225.

Cutnell, J. D., & Johnson, K. W. (2009). Physics 8e.

Dang, S., Yi, Y., & Ye, H. (2020). A visible transparent solar infrared reflecting film with a low long-wave emittance. *Solar Energy*, *195*, 483-490.

De Piante, M., & Tonello, A. M. (2016). On impedance matching in a power-line-communication system. *IEEE Transactions on Circuits and Systems II: Express Briefs*, *63*(7), 653-657.

Dubey, R. S., & Ganesan, V. (2017). Fabrication and characterization of TiO2/SiO2 based Bragg reflectors for light trapping applications. *Results in physics*, *7*, 2271-2276.

Fan, J., Liu, X., Furdyna, J. K., & Zhang, Y. H. (2012). ZnTe/GaSb distributed Bragg reflectors grown on GaSb for mid-wave infrared optoelectronic

George, S. M. (2010). Atomic layer deposition: an overview. *Chemical reviews*, *110*(1), 111-131.

Gill, G. S., Tripathi, D. K., Keating, A., Putrino, G., Silva, K. K. M. B. D., Martyniuk, M., & Faraone, L. (2022). Ge/BaF2 thin-films for surface micromachined mid-wave and long-wave infrared reflectors. *Journal of Optical Microsystems*, *2*(1), 011002-011002.

Guo, Z., Liu, X., Li, C., Li, J., Cai, H., Fu, M., ... & Wang, Y. (2021). Near-perfect broadband metamaterial absorbers of truncated nanocones using colloidal lithography. *Optical Materials*, *119*, 111352.

Heavens, O. S. (1986). Thin-film optical filters. *Optica Acta: International Journal of Optics*, *33*(11), 1336-1336.

Hinczewski, D. S., Hinczewski, M., Tepehan, F. Z., & Tepehan, G. G. (2005). Optical filters from SiO2 and TiO2 multi-layers using sol–gel spin coating method. *Solar energy materials and solar cells*, *87*(1-4), 181-196.

Howell, J. R., Mengüç, M. P., Daun, K., & Siegel, R. (2020). *Thermal radiation heat transfer*. CRC press.

Huo, D., Zhang, J., Wang, Y., Wang, C., Su, H., & Zhao, H. (2018). Broadband perfect absorber based on TiN-nanocone metasurface. *Nanomaterials*, *8*(7), 485.

Jain, P. K., Lee, K. S., El-Sayed, I. H., & El-Sayed, M. A. (2006). Calculated absorption and scattering properties of gold nanoparticles of different size, shape, and composition: applications in biological imaging and biomedicine. *The journal of physical chemistry B*, *110*(14), 7238-7248.

Jäger, K., Sutter, J., Hammerschmidt, M., Schneider, P. I., & Becker, C. (2021). Prospects of light management in perovskite/silicon tandem solar cells. *Nanophotonics, 10*(8), 1991-2000.

Karimi Habil, M., Ghahremani, M., & Zapata–Rodríguez, C. J. (2022). Multi-octave metasurface-based refractory superabsorber enhanced by a tapered unit-cell structure. Scientific Reports, 12(1), 17066.

Keçebaş, M. A. (2016). *Passive radiative cooling using optical thin film coatings* (Doctoral dissertation).

Keçebaş, M. A. (2020). *Design of spectrally selective surfaces* (Doctoral dissertation).

Kelly, K. L., Coronado, E., Zhao, L. L., & Schatz, G. C. (2003). The optical properties of metal nanoparticles: the influence of size, shape, and dielectric environment. *The Journal of Physical Chemistry B*, *107*(3), 668-677.

Ko, Y. H., & Magnusson, R. (2024, November). Double-Sided Metasurfaces for Dual-Band Mid-Wave and Long-Wave Infrared Reflectors. In *Photonics* (Vol. 11, No.

12, p. 1132). MDPI.

Kong, X., Sun, H., Liang, S., Yi, Z., Gu, N., & Yi, Y. (2024). Intelligent Space Thermal Control Radiator Based on Phase Change Material with Partial Visible Transparency. *Coatings*, *14*(5), 535.

Koucheh, A. B., Kecebas, M. A., & Sendur, K. (2021). Impedance mismatch-based enhancement of broadband reflectance of tungsten with bio-inspired multilayers. *Journal of Quantitative Spectroscopy and Radiative Transfer*, *276*, 107899.

Kyal, C. K., Poddar, H., & Reza, M. (2018, December). Detection of human face by thermal infrared camera using MPI model and feature extraction method. In *2018 4th International Conference on Computing Communication and Automation (ICCCA)* (pp. 1-5). IEEE.

Lee, H. J., Park, J. Y., Kwac, L. K., & Lee, J. (2024). Improvement of Near-Infrared Light-Emitting Diodes' Optical Efficiency Using a Broadband Distributed Bragg Reflector with an AlAs Buffer. *Nanomaterials*, *14*(4), 349.

Leem, J. W., Guan, X. Y., & Yu, J. S. (2014). Tunable distributed Bragg reflectors with wide-angle and broadband high-reflectivity using nanoporous/dense titanium dioxide film stacks for visible wavelength applications. *Optics Express*, *22*(15), 18519-18526.

Letka, V., Bainbridge, A., Craig, A. P., Al-Saymari, F., & Marshall, A. R. (2019). Resonant cavity-enhanced photodetector incorporating a type-II superlattice to extend MWIR sensitivity. *Optics Express*, *27*(17), 23970-23980.

Liu, J., Liu, D., Shen, Y., Yang, X., Zhao, C., Chen, R., ... & Xiao, H. (2020). Fabrication and applications of wafer-scale nanoporous GaN near-infrared distributed Bragg reflectors. *Optical Materials*, *107*, 110093.

Liu, Y., Liu, A., Chai, X., Yang, Y., Lu, M., Bai, X., ... & Zhang, Y. (2024). An interesting functional phase change material VO2: response to multivariate control and extensive applications in optics and electronics. *Advanced Electronic Materials, 10*(4), 2300699.

Long, M., Wang, Y., Wang, P., Zhou, X., Xia, H., Luo, C., ... & Hu, W. (2019). Palladium diselenide long-wavelength infrared photodetector with high sensitivity and stability. *Acs Nano*, *13*(2), 2511-2519.

Lu, Y. C., & Hsueh, C. H. (2024). Simulations and experimental studies of thermochromic performances of multilayered VO2 nanocone array for energy-

saving smart window applications. *Applied Surface Science*, *661*, 160083.

Markos, P., & Soukoulis, C. M. (2008). Wave propagation: from electrons to photonic crystals and left-handed materials. In *Wave Propagation*. Princeton University Press.

Mikulicz, M., Badura, M., Rygała, M., Smołka, T., Macherzyński, W., Łozińska, A., & Motyka, M. (2024). Development of the hybrid distributed Bragg reflectors for mid-infrared applications. *Opto-Electronics Review*, e149168-e149168.

Mrázek, J., Spanhel, L., Matějec, V., Bartoň, I., Džunda, R., & Puchý, V. (2021). Nanocrystalline Zn2TiO4 films for distributed Bragg's reflectors operating in near infrared region. *Optical Materials*, *112*, 110805.
applications. *Applied Physics Letters*, *101*(12).

Nakano, M., Shibuya, K., Okuyama, D., Hatano, T., Ono, S., Kawasaki, M., ... & Tokura, Y. (2012). Collective bulk carrier delocalization driven by electrostatic surface charge accumulation. *Nature*, *487*(7408), 459-462.

Obraztsov, A. N., Obraztsova, E. A., Tyurnina, A. V., & Zolotukhin, A. A. (2007). Chemical vapor deposition of thin graphite films of nanometer thickness. *Carbon*, *45*(10), 2017-2021.

Palik, E. D. (Ed.). (1998). *Handbook of optical constants of solids* (Vol. 3). Academic press.

Perego, M., Fanciulli, M., Bonafos, C., & Cherkashin, N. (2006). Synthesis of mono and bi-layer of Si nanocrystals embedded in a dielectric matrix by e-beam evaporation of SiO/SiO2 thin films. *Materials Science and Engineering: C*, *26*(5-7), 835-839.

Pirouzfam, N., & Sendur, K. (2021). Tungsten based spectrally selective absorbers with anisotropic rough surface texture. *Nanomaterials*, *11*(8), 2018.

Quazi, M. M., Fazal, M. A., Haseeb, A. S. M. A., Yusof, F., Masjuki, H. H., & Arslan, A. (2016). Laser-based surface modifications of aluminum and its alloys. *Critical Reviews in Solid State and Materials Sciences*, *41*(2), 106-131.

R. C. Rumpf, «www.empossible.com,» EMPossible, [Online]. Available: https://empossible.net/academics/emp5304/. [Accessed: 02 12 2021].

Rabaste, S., Bellessa, J., Brioude, A., Bovier, C., Plénet, J. C., Brenier, R., ... & Dumas, J. (2002). Sol–gel fabrication of thick multilayers applied to Bragg reflectors and microcavities. *Thin Solid Films*, *416*(1-2), 242-247.

Razi, A., Safdar, A., & Irfan, R. (2023). Optical optimization of tandem solar cells: a

systematic review for enhanced power conversion. *Nanomaterials*, *13*(23), 2985.

Rissanen, A., & Puurunen, R. L. (2012, February). Use of ALD thin film Bragg mirror stacks in tuneable visible light MEMS Fabry-Perot interferometers. In *Advanced Fabrication Technologies for Micro/Nano Optics and Photonics V* (Vol. 8249, pp. 252-260). SPIE.

Shim, H. B., Han, K., Song, J., & Hahn, J. W. (2022). A multispectral single-layer frequency selective surface absorber for infrared and millimeter wave selective bi-stealth. *Advanced Optical Materials*, *10*(6), 2102107.

Sugawara, H., Itaya, K., & Hatakoshi, G. (1993). Characteristics of a distributed Bragg reflector for the visible-light spectral region using InGaAlP and GaAs: Comparison of transparent-and loss-type structures. *Journal of applied physics*, *74*(5), 3189-3193.

Tripathi, D. K., Mao, H., Silva, K. D., Bumgarner, J. W., Martyniuk, M., Dell, J. M., & Faraone, L. (2015). Large-area MEMS-based distributed Bragg reflectors for short-wave and mid-wave infrared hyperspectral imaging applications. *Journal of microelectromechanical systems*, *24*(6), 2136-2144.

Wang, J., Liang, Y., Huo, P., Wang, D., Tan, J., & Xu, T. (2017). Large-scale broadband absorber based on metallic tungsten nanocone structure. *Applied Physics Letters*, *111*(25).

Wang, J., Sun, J., Guo, T., Zhang, H., Xie, M., Yang, J., ... & Bai, S. (2022). High-strength flexible membrane with rational pore architecture as a selective radiator for high-efficiency daytime radiative cooling. *Advanced Materials Technologies*, *7*(1),

Weiwei, Z. (2012). Impedance Matching Circuit Principle and its Application. *Electronic Science and Technology*.

Whittaker, L., Jaye, C., Fu, Z., Fischer, D. A., & Banerjee, S. (2009). Depressed phase transition in solution-grown VO2 nanostructures. *Journal of the American Chemical Society*, *131*(25), 8884-8894.

Williams, C., Hong, N., Julian, M., Borg, S., & Kim, H. J. (2020). Tunable mid-wave infrared Fabry-Perot bandpass filters using phase-change GeSbTe. *Optics Express*, *28*(7), 10583-10594.
2100528.

Xie, B., Song, Y., Chen, S., & Liu, L. (2025). Wavelength-selective emitter compatible with multiband stealth and dual-band heat dissipation. Applied Thermal

Engineering, 267, 125805.

Xu, G., Kang, Q., Zhang, X., Wang, W., Guo, K., & Guo, Z. (2024). Inverse-design laser-infrared compatible stealth with thermal management enabled by wavelength-selective thermal emitter. *Applied Thermal Engineering*, *255*, 124063.

Yang, J., Li, D., Wang, X., Jin, H., & Li, J. (2022). Optimizing phase transition temperature and visible transmittance of VO2 films driven by synergistic effect of La-Mo co-doping. *Applied Surface Science*, *600*, 154074.

Yee, K. (1966). Numerical solution of initial boundary value problems involving Maxwell's equations in isotropic media. *IEEE Transactions on antennas and propagation*, *14*(3), 302-307.